THE ASTROPHYSICAL JOURNAL, 470:1033–1051, 1996 October 20

MOTION OF ACCRETING MATTER NEAR LUMINOUS SLOWLY ROTATING RELATIVISTIC STARS

M. COLEMAN MILLER[1]
Department of Astronomy and Astrophysics, University of Chicago, 5640 South Ellis Avenue, Chicago, IL 60637;
miller@gamma.uchicago.edu

AND

FREDERICK K. LAMB[2]
Department of Physics, University of Illinois at Urbana-Champaign, 1110 West Green Street, Urbana, IL 61801-3080;
f-lamb@uiuc.edu

Received 1995 June 26; accepted 1995 September 28

ABSTRACT

In a previous paper, we reported test particle calculations showing that the behavior of accretion flows near uniformly emitting, nonrotating, relativistic stars is affected significantly by radiation forces if the luminosity is greater than $\sim 1\%$ of the Eddington critical luminosity L_E. Here, using a numerical code that can follow the motion of a test particle in any stationary axisymmetric spacetime, we investigate the effects of nonuniform emission and of slow rotation of the gravitating mass and radiation source, when their rotation axes are co-aligned. We find that for emission from a bright, thin ring, accreting particles are braked sharply near the radiation source, which may be favorable for the development of shock waves. We also show that if the particle orbit is prograde with respect to the rotation of the radiation source, the rates at which energy and angular momentum are lost to the radiation field are less than the rates for a nonrotating source. The diminished loss rates lead to a lower inward radial velocity, which increases the infall time. Surprisingly, if the radiation flux is sufficiently small, the increase in the infall time more than compensates for the decrease in the loss rates, so the total energy and angular momentum transferred to the radiation field during particle inspiral are actually greater than for a nonrotating radiation source. We also discuss some of the effects of radiation forces on accreting fluid. We show that the angular, special relativistic, and general relativistic effects that augment radiation drag on test particles near radiating relativistic stars also increase the fraction of angular momentum and energy that can be transferred from the accretion flow to the radiation field. This may affect the maximum rotation rate of neutron stars and the prospects for observing gravitational radiation from rapidly rotating neutron stars.

Subject headings: accretion, accretion disks — black hole physics — relativity — stars: neutron

1. INTRODUCTION

Most energetic astrophysical X-ray sources, such as active galactic nuclei and low-mass X-ray binaries (LMXBs), are powered by accretion. In many cases the luminosity is a substantial fraction of the Eddington critical luminosity L_E at which the outward radiation force balances gravity. Even if the luminosity is as low as $0.01L_E$, radiation drag can affect the behavior of the accretion flow close to the central neutron star or black hole (Miller & Lamb 1993, hereafter ML93). Thus neglect of radiation forces in calculations of accretion flows near black holes and relativistic stars (see, e.g., Kluzniak & Wagoner 1985; Sunyaev & Shakura 1986; Hanawa 1989; Fu & Taam 1990; Czerny, Czerny, & Grindlay 1986; Ebisawa, Mitsuda, & Hanawa 1991; Kluzniak & Wilson 1991; Biehle & Blandford 1993) is usually inappropriate. Previous calculations of accretion flows near relativistic stars have generally also assumed either Newtonian gravity or, if general relativistic, the exterior Schwarzschild spacetime geometry; however, in many cases the accreting object may have been spun up before or during its accretion phase to rotation rates that cause the spacetime geometry to deviate significantly from the Schwarzschild geometry. The appropriate, more general spacetime geometry must then be considered.

We have developed a numerical code that incorporates ray-tracing in a general, stationary, axisymmetric spacetime and can treat the effects of radiation forces on equatorial test particle motion around axisymmetric relativistic objects such as neutron stars and black holes. In the test particle approximation, the spacetime and radiation stress-energy tensor are assumed fixed and unaffected by the accreting particle. For simplicity, we assume that only gravitational and radiation forces act on the particle. Although many of the analytical and numerical results presented here are for slowly rotating objects, the code makes no such approximation and can therefore be used to study test particle motion around rapidly rotating relativistic stars and black holes. The first applications of this code were reported in ML93, where we studied the motion of test particles near nonrotating neutron stars by calculating trajectories in the presence of radiation in the Schwarzschild spacetime. In that work we assumed that the radiation source was a nonrotating, isotropically radiating sphere. We found that near luminous sources, radiation forces strongly affect the motion of accreting matter, the luminosity of any boundary layer at the steller surface, and the specific angular momentum accreted by the star. We showed that for luminosities $L > 0.01L_E$, radiation forces are more important than general relativistic corrections to

[1] *Compton Gamma-Ray Observatory* Fellow.
[2] Also, Department of Astronomy, University of Illinois at Urbana-Champaign.

Newtonian gravitational forces in determining the behavior of the accretion flow.

In the present paper we develop a framework for computing test particle motion in the presence of radiation in stationary, axisymmetric spacetimes, such as those produced by rotating neutron stars and black holes. We then use this framework to study test particle motion around slowly rotating neutron stars with various radiation patterns. We assume that the rotation axes of the gravitating mass and of the radiating matter are co-aligned. The results presented here are applicable to all neutron stars with measured rotation rates. The analytical results obtained here provide a check on the numerical results obtained with our more general code. In subsequent papers we will report results obtained by applying this framework to test particle motion in the presence of radiation near black holes and rapidly rotating neutron stars.

The computations presented here extend those reported in ML93 by treating radiation from boundary layers with half-widths ranging from 100% of the stellar radius (which reproduces a spherically symmetric source) to 10% of the radius. The smaller half-widths simulate the radiation pattern expected if the star is accreting from a geometrically thin disk and most of the radiation is emitted from a thin band around the stellar equator.

The computations presented here also extend those reported in ML93 by including rotation of the gravitating mass and radiating matter, which introduces two distinct effects. If the gravitating mass is rotating, the exterior geometry deviates from the Schwarzschild geometry. If the radiating matter has an azimuthal velocity $v^{\hat{\phi}}$ (as measured in the locally nonrotating frame [LNRF]; see Bardeen 1970; Bardeen, Press, & Teukolsky 1972), the resulting Doppler shifts will cause the radiation field from even a spherical radiating surface to be anisotropic. Both effects alter the motion of particles near the star. A convenient measure of the rotation rate of the gravitating mass is the dimensionless angular momentum $j \equiv cJ/(GM^2)$, where J is its angular momentum, M is its gravitational mass, G is the gravitational constant, and c is the speed of light. A similarly convenient measure of the rotation rate of the radiating matter is the dimensionless velocity $v \equiv \langle v^{\hat{\phi}} \rangle / c$, where $\langle v^{\hat{\phi}} \rangle$ is the appropriate average of $v^{\hat{\phi}}$ over the emitting matter (see § 6). Most of the analytical results reported in this paper assume slow rotation ($j \ll 1$ and $v \ll 1$) and retain only terms that are first-order in j and v. Keeping only terms to first order in v is expected to be a good approximation if the neutron star is slowly rotating (see Lamb & Miller 1995, hereafter LM95), and we now argue that for neutron stars with measured spin rates, retaining only terms to first order in j is an excellent approximation.

The two fastest rotation-powered pulsars both have spin frequencies $\nu_s \approx 600$ Hz (see Taylor et al. 1995). For a slowly rotating (and therefore approximately spherical), uniform-density neutron star with angular frequency Ω, $J \approx (2/5)MR^2\Omega$. Hence, a star of radius $R \approx 10$ km, mass $M \approx 1.4\ M_\odot$, and $\nu_s \approx 600$ Hz has $j \approx 0.2$. Most rotation-powered pulsars have much smaller values of j. The fastest known accretion-powered pulsar has a spin frequency ≈ 16 Hz (van Paradijs 1991) and hence $j \approx 0.005$. It is possible, however, that there is a population of very rapidly spinning, rotation-powered pulsars that are either too fast or too faint to be detected by current surveys. It is also plausible that in many neutron star LMXBs the stellar spin frequency is difficult to detect because of obscuring plasma. If the magnetic fields of some of these neutron stars are very weak, accretion could spin them up to values of j large enough that effects nonlinear in j are important. Thus, although a first-order treatment of rotation encompasses all known neutron star spin rates, rapidly rotating neutron stars may be important; they will be treated in a future paper.

We find that for a particle in prograde orbit around rotating, radiating matter, the *rates* at which the particle loses energy and angular momentum to the radiation field are *smaller* than they would be if the radiating matter were not rotating (the rotation of the gravitating mass is much less important). Nevertheless, for low enough radiation fluxes, the *total* energy and angular momentum transferred to the radiation during particle inspiral is *larger*. This surprising result is caused by the increase in the infall time, which more than compensates for the smaller energy and angular momentum loss rates. We also find that for emission from a bright, thin ring, orbiting particles are sharply braked near the radiation source, where the radiation flux rises sharply.

The relativistic equation of motion and our numerical method are described in § 2. In § 3 we summarize the main results of ML93 and compare the analytical expressions given there for the loss rates of energy and angular momentum with the loss rates given by our numerical code. In § 4 we calculate the radiation stress-energy tensor produced by rotating radiation sources in the exterior Schwarzschild spacetime and compute the equilibrium angular momentum as a function of radius. In § 5 we derive the equations that describe free fall using a metric that is accurate to first order in the rotation rate of the gravitating mass and compare these analytical results with the trajectories given by our numerical code, which does not assume slow rotation. We also calculate exact free-fall trajectories in the Kerr metric for a sequence of j values ranging up to $j = 0.9$ and compare these trajectories with the trajectories given by our numerical code. In § 6 we study analytically the radiation field around slowly rotating radiating matter in the spacetime exterior to a slowly rotating gravitating mass and derive formulae for the apparent angular shape of the star, the photon frequency shifts caused by Doppler shifts and frame-dragging, and the off-diagonal components of the radiation stress-energy tensor. In § 7 we use our numerical code to study the motion of test particles exposed to the radiation produced by slowly rotating radiating matter in the spacetime exterior to a slowly rotating gravitating mass. We summarize our results and discuss their application to X-ray burst sources, accreting neutron stars, and the spin-up of neutron stars in § 8.

2. EQUATION OF MOTION AND NUMERICAL METHOD

All the calculations of particle motion in this paper are performed in the test particle approximation, i.e., the spacetime and radiation stress-energy tensor are assumed fixed and unaffected by the particles. The source of gravity is assumed to be an axisymmetric, rotating, compact object. The only nongravitational force we consider is that exerted by the radiation. Test particles are assumed to scatter radiation, with a momentum-transfer cross section that is independent of photon energy and direction. The radiation force on the scattering particle is therefore proportional to and in the direction of the radiation flux in the comoving frame (see LM95). The relevant properties of the test particle are

its rest mass m and scattering cross section σ, although in applications of our results the "particle" need not be a single object. For example, close to an accreting neutron star, matter is likely to consist largely of fully ionized hydrogen at temperatures of a few keV. Under these conditions, the electrons and protons are electrically coupled together, and the plasma can therefore be treated as composed of particles with rest mass $m \approx m_p$, the proton mass, and momentum-transfer cross section $\sigma \approx \sigma_T$, the electron Thomson cross section (see LM95).

2.1. *Equation of Motion*

The relativistic equation of motion determines the orbits of test particles. To derive this equation, we follow closely the notation and approach of Abramowicz, Ellis, & Lanza (1990, hereafter AEL), who studied radial particle motion in the Schwarzschild geometry. We generalize their treatment to arbitrary equatorial motion in an arbitrary axisymmetric spacetime. Unlike AEL, we use the metric signature $-+++$, so there are some sign differences between our expressions and theirs. The exterior metric of a rapidly rotating neutron star deviates significantly from the Kerr metric (Friedman, Ipser, & Parker 1986; Cook, Shapiro, & Teukolsky 1994), so we use the general axisymmetric metric employed by Bardeen (1970) and Bardeen et al. (1972), i.e.,

$$ds^2 = g_{\alpha\beta}\,dx^\alpha dx^\beta = -e^{2\nu}dt^2 + e^{2\psi}(d\phi - \omega dt)^2 + e^{2\mu_1}dr^2 + e^{2\mu_2}d\theta^2 \,. \quad (1)$$

Here $\omega = \omega(r, \theta)$ is the angular velocity of the LNRF, a reference frame introduced by Bardeen in which the effects of frame-dragging are minimized. Here and below we set $c = G = 1$ except where noted and use the Einstein summation convention.

As usual, we denote tetrad quantities (i.e., quantities measured in a local orthonormal frame) by hats over the indices (e.g., $u^{\hat{r}}$ for the radial component of velocity) and quantities measured in Boyer-Lindquist coordinates by unhatted indices (e.g., u^r). In most cases in this paper, the only tetrads we consider are in the LNRF. We will frequently need to transform between the LNRF and Boyer-Lindquist coordinates. We denote the transformation tensor between these coordinates by $e^\alpha_{\hat{\nu}}$ and $e^{\hat{\alpha}}_\nu$ so, for example, $u^\alpha = e^\alpha_{\hat{\nu}}\, u^{\hat{\nu}}$. For the metric (1), the nonzero components of the transformation tensors are (Bardeen 1970)

$$e^t_{\hat{t}} = e^{-\nu}\,,\quad e^\phi_{\hat{t}} = \omega e^{-\nu}\,,\quad e^r_{\hat{r}} = e^{-\mu_1}\,,\quad e^\theta_{\hat{\theta}} = e^{-\mu_2}\,,\quad e^\phi_{\hat{\phi}} = e^{-\psi}\,;$$
$$e^{\hat{t}}_t = e^{\nu}\,,\quad e^{\hat{r}}_r = e^{\mu_1}\,,\quad e^{\hat{\theta}}_\theta = e^{\mu_2}\,,\quad e^{\hat{\phi}}_t = -\omega e^{\psi}\,,\quad e^{\hat{\phi}}_\phi = e^{\psi}\,. \quad (2)$$

Of these, only $e^\phi_{\hat{t}}$ and $e^{\hat{\phi}}_t$ depend on j to first order.

The relativistic equation of motion is

$$a^\alpha = f^\alpha/m\,, \quad (3)$$

where f^α includes all of the nongravitational forces, m is the rest mass of the test particle, and

$$a^\alpha = \frac{d^2x^\alpha}{d\tau^2} + \Gamma^\alpha_{\mu\nu}u^\mu u^\nu \quad (4)$$

is the acceleration. In equation (4) $\boldsymbol{u}$ is the four-velocity (u_ϕ is the specific angular momentum and $-u_t$ is the specific energy), τ is the proper time,

$$\Gamma^\alpha_{\mu\nu} = \tfrac{1}{2}g^{\alpha\beta}(g_{\beta\mu,\nu} + g_{\beta\nu,\mu} - g_{\mu\nu,\beta}) \quad (5)$$

are the connection coefficients, and commas denote partial derivatives. With our choice of metric signature, the squared four-velocity $\boldsymbol{u}^2$ is zero for massless particles and -1 for massive particles.

If the only nongravitational force is that due to scattering of radiation and the momentum-transfer cross section σ of the particle is independent of the direction and frequency of the radiation, then (see LM95)

$$f^\alpha = \sigma F^\alpha \quad (6)$$

where F^α is the radiative energy flux measured in the rest frame of the particle and is given by

$$F^\alpha = h^\alpha_\beta\, T^{\mu\beta}u_\mu\,. \quad (7)$$

Here $T^{\mu\beta}$ is the stress-energy tensor of the radiation and

$$h^\alpha_\beta = -\delta^\alpha_\beta - u^\alpha u_\beta \quad (8)$$

is a tensor that projects orthogonally to the four-velocity. Thus, to follow the motion of a test particle we need only compute the relevant components of $T^{\mu\nu}$ at the particle.

The components of the radiation stress-energy tensor at a given event in the Boyer-Lindquist coordinate system are related to the components in the LNRF tetrad by

$$T^{\alpha\beta} = e^\alpha_{\hat{\mu}}\, e^\beta_{\hat{\nu}}\; T^{\hat{\mu}\hat{\nu}}\,. \quad (9)$$

We define right-handed coordinate axes ($\hat{r}$, $\hat{\theta}$, $\hat{\phi}$) (note that AEL used left-handed axes) in the local sky of the observer such that $\hat{r}$ is in the *negative* radial direction, $\hat{\phi}$ is in the positive ϕ direction, and $\hat{\theta}$ is along the positive θ direction. Following AEL, we define local angles $\tilde{a}$ and $\tilde{b}$ such that an element of solid angle is $d\tilde{\Omega} = \sin\tilde{a}\,d\tilde{a}\,d\tilde{b}$. We also define a unit spacelike vector $n^{\hat{\alpha}} = u^{\hat{\alpha}}/u^{\hat{t}}$. Then

$$n^{\hat{r}} = \cos\tilde{a}\,,\quad n^{\hat{\theta}} = \sin\tilde{a}\cos\tilde{b}\,,\quad \text{and}\quad n^{\hat{\phi}} = \sin\tilde{a}\sin\tilde{b}\,. \quad (10)$$

The quantity $\tilde{b}$ is defined so that $\tilde{b} = \pi/2$ in the positive ϕ direction. With these definitions,

$$T^{\hat{\alpha}\hat{\beta}} = \int I(r, \theta, \tilde{a}, \tilde{b})n^{\hat{\alpha}}n^{\hat{\beta}}\,d\tilde{\Omega}\,, \quad (11)$$

where $I(r, \theta, \tilde{a}, \tilde{b})$ is the frequency-integrated specific intensity in the direction $\tilde{a}$, $\tilde{b}$ at the position (r, θ) of the test particle.

Since I/ν^4 is conserved along ray paths, where ν is the frequency of a photon, the relation between the received and the emitted frequency-integrated specific intensity is

$$I_r = \left(\frac{\nu_r}{\nu_e}\right)^4 I_e\,, \quad (12)$$

where ν_e and ν_r are, respectively, the emitted and received frequencies of a given photon. Calculation of the specific intensity needed to evaluate the components of the stress-energy tensor using equation (11) thus reduces to keeping track of the change in the photon frequency along the ray path from the source to the test particle. There can be several sources of frequency shift. For a nonrotating, spherical radiation source in Schwarzschild spacetime, only the gravitational redshift is involved (see § 3). For a rotating boundary layer in Schwarzschild spacetime, Doppler shifts must also be included (see § 4). Finally, if the gravitating mass is itself rotating, frame-dragging effects change the frequency of the photon (see § 6). Although the specific dependence of the frequency shift on the direction of the ray

at the test particle depends on the details of the situation, the approach just described can always be used.

For simplicity, in calculating $T^{\hat{\alpha}\hat{\beta}}$ we assume that the specific intensity I_s at the source as measured in the rest frame of the radiating matter is independent of the angle to the normal (see LM95 for a discussion), but we allow I_s to depend on the colatitude θ of the radiating matter (since the program keeps track of the spatial location $[r, \theta]$ of the points on the ray path, it is straightforward to consider an I_s that depends on colatitude). We can, therefore, treat the case of a bright equatorial band as well as the case of an isotropically emitting spherical radiation source.

2.2. *Numerical Method*

If the source geometry is sufficiently simple, analytical expressions can be derived for the stress-energy tensor, the drag force, energy loss rates, the apparent shape of the radiation source, and other important quantities. Some of these analytical solutions are presented in the next four sections. However, in general numerical methods must be used. Here we describe our method. In subsequent sections we indicate how well our numerical results agree with the corresponding analytical results.

The full algorithm separates into two parts: we first calculate the stress-energy tensor using ray tracing and then use the components of the stress-energy tensor to determine the particle motion. The metric is specified on an r, θ grid (for particle motion in the equatorial plane only $\theta = \pi/2$ is relevant, but calculation of the luminosity requires computation of the radiation flux over the full range of θ at large r). A grid spacing of $0.2M$ in r gives satisfactory accuracy everywhere. The number N_θ of angular zones depends on the spacetime geometry (the Schwarzschild geometry is independent of θ, but for a rapidly rotating star $N_\theta = 64$ may be required). The derivatives of the metric components, which are needed to compute the connection coefficients, are calculated with a bicubic spline at the same grid points at which the metric is specified. The transformation tensors $e^{\alpha}_{\hat{\nu}}$ are also calculated from the metric. Between grid points, we use a bilinear interpolation to compute metric components, derivatives of metric components, and transformation tensors. The simple interpolations and grid spacings we use allow us to quickly explore parameter space with relatively high accuracy, as shown by comparisons with our analytical results.

We begin the calculation of $T^{\hat{\alpha}\hat{\beta}}$ at the particle, where we define the local angles $\tilde{a}$ and $\tilde{b}$ as above. For a given local direction $(\tilde{a}, \tilde{b})$ of a light ray, the Boyer-Lindquist velocity components u^r, u^ϕ, and u^θ of the photon are computed and the null geodesic is traced backward along the ray path. Initially the specific energy $-u_t$ is calculated using $u^\alpha u_\alpha = 0$, but in the subsequent ray tracing the geodesic equation $a^\alpha = 0$ is integrated independently for all four components, so that the agreement of $\boldsymbol{u}^2$ with 0 provides a test of the accuracy of the ray tracing. For all of the rays generated in the tests reported here, $\boldsymbol{u}^2 < 0.02$; typically $\boldsymbol{u}^2 < 0.01$. The time step used in ray tracing is $0.01M$ in proper time, and the integration is performed using a trapezoidal rule.

A given ray is traced backward until either it intersects the emitting surface or it can be demonstrated that the ray did not originate from the radiation source. The exact criteria by which these are decided depend on the nature of the source. For example, if the source is a uniformly emitting, nonrotating sphere of radius $R > 3M$, the ray intersects the source when $r = R$ but will never intersect the source if $r > R$ and $dr/d\lambda > 0$ where λ is an affine parameter. Other source geometries require more complex criteria.

Once the origin of the ray is determined, calculation of $T^{\hat{\alpha}\hat{\beta}}$ requires computation of the specific intensity of the ray at the particle. If the ray does not intersect the radiation source, $I = 0$. If the ray does intersect the source, the specific intensity at the particle is a function of both the specific intensity I_s at the source and the frequency shift from the source to the test particle.

As discussed above, the frequency shift from the source to the LNRF at the particle may be computed by considering separately the Doppler shift between the source and the LNRF at the source, and the shift between the LNRF at the source and the LNRF at the particle. The Doppler shift at the source can be determined by computing the velocity v of the source as seen by an observer in the LNRF at the source and then using special relativity; the LNRF frequency shift can be calculated from the metric. In general, an accreting particle at r is not at rest in the LNRF there. Hence, after computing $T^{\hat{\alpha}\hat{\beta}}$ in the LNRF at the particle, we transform into the Boyer-Lindquist cordinate system and use the equations of § 2.1 to compute the motion of the particle in the Boyer-Lindquist coordinate system.

Since we are considering only particle motion in the equatorial plane, near the source we only need to compute the radiation stress-energy tensor at $\theta = \pi/2$. Since the system is assumed to be axisymmetric, we do not need to consider variation of the stress-energy tensor with ϕ. For simplicity, $T^{\hat{\alpha}\hat{\beta}}$ is calculated at the grid points where the metric is specified. We find that a grid of approximately 2000 local angular zones (60 in $\tilde{b}$, 30 in $\tilde{a}$) suffices for all our purposes, if the ranges of $\tilde{a}$ and $\tilde{b}$ are chosen properly. For example, if the radiation source is a slowly rotating sphere, the maximum extent of $\tilde{a}$ can be estimated as a function of $\tilde{b}$ (see § 6 for details), allowing us to determine which ray directions should be considered to efficiently sample the entire radiation source.

Once the radiation stress-energy tensor has been computed, the particle motion is calculated by numerical integration of the equation of motion (3). Initially, the particle's position and velocity are specified and the specific energy u_t is computed from $\boldsymbol{u}^2 = -1$. Again, in following the motion of the particle all four components of its four-velocity are calculated independently, so that agreement with $\boldsymbol{u}^2 = -1$ is a test of the computational accuracy; this identity is always satisfied to better than 2%. As with the ray tracing, the time step is $0.01M$ in proper time, the integration is performed with a trapezoidal rule, and all interpolations are bilinear. The motion of the particle is followed until some stopping condition is reached, e.g., the particle hits the surface of the star. Tests of the accuracy of the numerical algorithm for specific cases may be found in the next three sections.

3. NONROTATING SPHERICAL RADIATION SOURCE IN SCHWARZSCHILD SPACETIME

In ML93 we considered some of the effects of radiation forces acting on test particles moving outside nonmagnetic, spherical, nonrotating relativistic stars. We showed that the radial and azimuthal velocities of infalling matter are affected significantly by radiation stresses if the luminosity of the star is greater than $\sim 0.01 L_{\rm E}^{\infty}$. For such luminosities, radiation forces dominate general relativistic corrections to

TABLE 1

DRAG RATES IN SCHWARZSCHILD SPACETIME

L^∞/L_E^∞	$dl_n \times 10^2$	$dl_a \times 10^2$	$de_n \times 10^3$	$de_a \times 10^3$
		$R = 4M, r_0 = 6M$		
0.05.....	0.39	0.39	0.96	0.91
0.2.....	1.50	1.46	2.86	2.85
0.5.....	3.36	3.30	3.48	3.47
		$R = 4M, r_0 = 9M$		
0.05.....	0.11	0.11	0.15	0.15
0.2.....	0.43	0.42	0.47	0.47
0.5.....	1.01	1.00	0.61	0.64
		$R = 5M, r_0 = 6M$		
0.05.....	0.45	0.45	1.07	1.06
0.2.....	1.71	1.70	3.30	3.31
0.5.....	3.86	3.83	3.95	4.04
		$R = 5M, r_0 = 9M$		
0.05.....	0.12	0.11	0.16	0.15
0.2.....	0.45	0.45	0.49	0.50
0.5.....	1.06	1.06	0.64	0.68

NOTE.—Comparison of the numerical and analytical estimates for the characteristic rates of removal of energy and angular momentum from test particles initially in circular orbits around a nonrotating, spherically symmetric radiation source in the Schwarzschild spacetime. The test particle is at an initial radius of either $r_0 = 6M$ or $r_0 = 9M$. The radiation source has a radius of either $R = 4M$ or $R = 5M$ and a luminosity at infinity of $L^\infty = 0.05L_E^\infty$, $L^\infty = 0.2L_E^\infty$, or $L^\infty = 0.5L_E^\infty$. In this table, dl stands for $-(du_\phi/d\tau)/u_\phi$, de stands for $-(de/d\tau)/e$ (where $e \equiv 1 - \tilde{E}_b$ is the specific energy), the subscript n indicates the numerical estimate, and the subscript a indicates the analytical estimate. In all cases the estimates agree well, with a maximum deviation of $\sim 5\%$.

Newtonian gravity, and hence there are no qualitative changes in the character of the motion at the radius of the innermost stable circular orbit.

For a uniformly emitting radiation source, the characteristic rates of transfer of specific angular momentum and specific binding energy to the radiation field from a particle in an initially circular orbit are (see Appendix A)

$$\frac{1}{\tilde{E}_b}\frac{d\tilde{E}_b}{d\tau} = +f(\alpha_0)\left(\frac{1-\tilde{E}_b}{\tilde{E}_b}\right)\frac{M\tilde{l}^2}{3R^2r^2}\frac{(1-2M/R)}{(1-2M/r)^2}\left(\frac{L^\infty}{L_E^\infty}\right) \quad (13)$$

and

$$\frac{1}{\tilde{l}}\frac{d\tilde{l}}{d\tau} = -f(\alpha_0)(1-\tilde{E}_b)^2\frac{M}{3R^2}\frac{(1-2M/R)}{(1-2M/r)^3}\left(\frac{L^\infty}{L_E^\infty}\right). \quad (14)$$

In both equations $\tilde{E}_b$ is the specific binding energy and $\tilde{l}$ is the specific angular momentum of the particle, M is the gravitational mass of the star, L^∞ is the luminosity at infinity, and $f(\alpha_0) \equiv (8 - 9\cos\alpha_0 + \cos^3\alpha_0)$, where α_0 is the apparent half-angle subtended by the radiation source and the subscript 0 indicates that the star is nonrotating. The Eddington critical luminosity

$$L_E^\infty \equiv 4\pi mM/\sigma \quad (15)$$

is the luminosity of a spherically symmetric source such that at infinity the outward force of radiation balances the inward force of gravity (see LM95 for the conditions under which L_E^∞ is a useful benchmark). Throughout this paper, R and r denote respectively the Boyer-Lindquist radius of the star and the radial position of the particle; for metrics that are not spherically symmetric these radii generally differ from the corresponding circumferential radii. For stars not more compact than the photon orbit (that is, with radii $R \geq 3M$), α_0 is given implicitly by

$$\sin\alpha_0 = \left(\frac{R}{r}\right)\left(\frac{1-2M/r}{1-2M/R}\right)^{1/2}. \quad (16)$$

Expression (14) includes three effects that are not present in the Newtonian, point-source approximation. These are discussed in detail in Appendix A. The first effect is the finite angular size of the source, which is described by the factor $f(\alpha_0)$, exactly the same angular factor that appears in the Newtonian approximation (Guess 1962). This effect can increase the drag force by up to a factor of 8/3 (contrary to the explanation given by Guess, much of the increase is due not to Doppler shifts but to the increase in the radiation energy density near a source of finite angular size). The second effect is special relativistic beaming of the scattered radiation, which can increase the drag force by up to a factor of about 4/3. Finally, the effects of general relativity, which include redshifts, frequency shifts, and angular defocusing, can increase the drag force by up to a factor of 2. These effects combine to increase dramatically the importance of radiation drag near a relativistic star. One measure of the qualitative impact of radiation drag is the ratio of the characteristic timescale for angular momentum loss to the orbital timescale, allowing for the increase in the orbital period caused by the radial component of the radiation force. At distances ~ 300 km from the star, the angular momentum of an orbiting particle is removed in less than one orbital period only for $L^\infty \gtrsim 0.95L_E^\infty$ (Fortner, Lamb, & Miller 1989); close to the star this occurs for $L^\infty \gtrsim 0.2L_E^\infty$.

We have used expressions (13) and (14) to check the accuracy of the rates of change of the energy and angular momentum of a particle given by our numerical code. Table 1 compares our numerical and analytical results for the characteristic rates of removal of energy and angular momentum from test particles initially in circular orbits at $6M$ and $9M$, for stars of radius $4M$ and $5M$. We consider three values of the luminosity at infinity: $L^\infty = 0.05L_E^\infty$, $0.2L_E^\infty$, and $0.5L_E^\infty$. The maximum difference is $\sim 5\%$. Note that the analytical derivatives are computed for perfectly circular orbits, whereas the numerical derivatives can be calculated only after there is a slight deviation from circularity. The tabulated numerical results will thus agree only approximately with these analytical results. We regard the agreement evident in Table 1 as an adequate verification of the accuracy of the code (had we used the analytical expressions for noncircular orbits given in Appendix A, we expect that the agreement would have been even better).

4. EQUILIBRIUM ANGULAR MOMENTUM NEAR ROTATING RADIATION SOURCES

Even if the gravitating mass is nonrotating and spherical, so that the geometry of spacetime is the Schwarzschild geometry, it is possible that most of the radiation comes from matter that has nonzero angular velocity. Then, Doppler shifts and aberration must be taken into account. We therefore consider now the effect on initially purely azimuthal particle motion of the radiation field produced by a boundary layer rotating slowly and uniformly around a spherical star. To account for the possibility that the boundary layer may not cover the entire star, we examine

both uniform emission from the whole stellar surface and uniform emission from a band of finite thickness around the equator. We concentrate on the properties of and asymptotic expressions for the *equilibrium angular momentum* $u_{\phi 0}$, which is the specific angular momentum of a particle in circular motion at which the azimuthal radiation force in the rest frame of the particle vanishes. This angular momentum depends only weakly on the radial position of the particle, and because the radiation force causes the angular momenta of inspiraling particles to tend to $u_{\phi 0}$, the equilibrium angular momentum introduces new, potentially observable, characteristic frequencies of motion near relativistic stars. In this section, we also show that one-dimensional rings have degenerate mathematical properties and therefore cannot be used to build up the pattern of emission from a finite band.

For a test particle in circular equatorial motion, the ϕ-component of the radiation force is (see eqs. [6]–[8])

$$f^{\phi} = \sigma\left[\frac{1}{r}\left(1+\frac{u_{\phi}^2}{r^2}\right)^{1/2}\left(1+2\,\frac{u_{\phi}^2}{r^2}\right)T^{\hat{t}\hat{\phi}} - \frac{u_{\phi}}{r^2}\left(1+\frac{u_{\phi}^2}{r^2}\right)(T^{\hat{r}\hat{r}}+T^{\hat{\phi}\hat{\phi}})\right]. \quad (17)$$

For $T^{\hat{t}\hat{\phi}}$ small, equation (17) implies that f^{ϕ} vanishes if u_{ϕ} is equal to $u_{\phi 0}$, where

$$u_{\phi 0} \approx \frac{rT^{\hat{t}\hat{\phi}}}{T^{\hat{r}\hat{r}}+T^{\hat{\phi}\hat{\phi}}}. \quad (18)$$

If the particle's angular momentum u_{ϕ} is not initially equal to $u_{\phi 0}$, it tends to $u_{\phi 0}$; however, for slowly rotating radiation sources the particle usually does not reach $u_{\phi 0}$ before hitting the stellar surface, though it may for rapidly rotating sources. Note that $u_{\phi 0}=0$ if $T^{\hat{t}\hat{\phi}}=0$. This is the case, for example, when the radiation source is nonrotating and emission is forward-backward symmetric with respect to ϕ.

We now compute the components of $T^{\hat{\alpha}\hat{\beta}}$ needed in equation (17). Suppose that photons seen coming from the direction $(\tilde{a},\tilde{b})$ by an observer at radius r are emitted from matter with azimuthal velocity $v^{\hat{\phi}}(\tilde{a},\tilde{b})$ as seen by a static observer at the emitting surface. If the local static observer observes the ray emitted at angle ψ relative to the direction of motion of the surface, the frequency of the radiation seen by the observer is

$$\nu_r = \frac{\nu_e}{\gamma[1-v^{\hat{\phi}}(\tilde{a},\tilde{b})\cos\psi]}, \quad (19)$$

where ν_e is the emitted frequency and $\gamma \equiv (1-[v^{\hat{\phi}}(\tilde{a},\tilde{b})]^2)^{-1/2}$ is unity, to first order in $v^{\hat{\phi}}(\tilde{a},\tilde{b})$. Since $\boldsymbol{v} \parallel \hat{\phi}$, finding $\cos\psi$ for photons that arrive at radius r from the local direction $(\tilde{a},\tilde{b})$ amounts to finding the ϕ component of the photon propagation direction at R, that is, $n^{\hat{\phi}}_R$. For an observer at radius r,

$$n^{\hat{\phi}} = \frac{u^{\hat{\phi}}}{u^{\hat{t}}} = \frac{(1/r)u_{\phi}}{-(1-2M/r)^{1/2}u_t} = \frac{R}{r}\frac{(1-2M/r)^{1/2}}{(1-2M/R)^{1/2}}n^{\hat{\phi}}_R = \frac{R}{r}\frac{(1-2M/r)^{1/2}}{(1-2M/R)^{1/2}}\cos\psi. \quad (20)$$

Since $n^{\hat{\phi}} = \sin\tilde{a}\sin\tilde{b}$, this means

$$\cos\psi = \frac{r}{R}\frac{(1-2M/R)^{1/2}}{(1-2M/r)^{1/2}}\sin\tilde{a}\sin\tilde{b}. \quad (21)$$

In addition to the Doppler shift, the photon frequency is also affected by the redshift from source to observer, which multiplies the frequency by a factor $(1-2M/R)^{1/2}/(1-2M/r)^{1/2}$. The frequency-integrated specific intensity $I \propto \nu^4$ and so to first order in $v^{\hat{\phi}}(\tilde{a},\tilde{b})$,

$$I(r,\tilde{a},\tilde{b}) \approx \frac{(1-2M/R)^2}{(1-2M/r)^2}\times\left[1+4v^{\hat{\phi}}(\tilde{a},\tilde{b})\frac{r}{R}\frac{(1-2M/R)^{1/2}}{(1-2M/r)^{1/2}}\sin\tilde{a}\sin\tilde{b}\right]I_s, \quad (22)$$

where I_s is the frequency-integrated specific intensity seen by an observer comoving with the radiating matter. Here and below we assume that I_s is independent of direction and uniform over the surface of the source where there is emission and zero otherwise. Thus, for a finite ring, I_s is a step function of θ.

To compute the components of $T^{\hat{\alpha}\hat{\beta}}$ required in equation (17) using equation (11), we must determine the boundaries of the source as seen at the accreting particle, for each of these geometries. For a uniformly radiating, two-dimensional source of arbitrary shape,

$$T^{\hat{r}\hat{r}} = I_s\frac{(1-2M/R)^2}{(1-2M/r)^2}\int_0^{2\pi}\int_0^{\alpha_0(\tilde{b})}\left[1+4v^{\hat{\phi}}(\tilde{a},\tilde{b})\times\frac{r}{R}\frac{(1-2M/R)^{1/2}}{(1-2M/r)^{1/2}}\sin\tilde{a}\sin\tilde{b}\right]\sin\tilde{a}\,d\tilde{a}\,d\tilde{b}, \quad (23)$$

$$T^{\hat{t}\hat{\phi}} = I_s\frac{(1-2M/R)^2}{(1-2M/r)^2}\int_0^{2\pi}\int_0^{\alpha_0(\tilde{b})}\left[1+4v^{\hat{\phi}}(\tilde{a},\tilde{b})\times\frac{r}{R}\frac{(1-2M/R)^{1/2}}{(1-2M/r)^{1/2}}\sin\tilde{a}\sin\tilde{b}\right]\sin^2\tilde{a}\sin\tilde{b}\,d\tilde{a}\,d\tilde{b}, \quad (24)$$

$$T^{\hat{\phi}\hat{\phi}} = I_s\frac{(1-2M/R)^2}{(1-2M/r)^2}\int_0^{2\pi}\int_0^{\alpha_0(\tilde{b})}\left[1+4v^{\hat{\phi}}(\tilde{a},\tilde{b})\times\frac{r}{R}\frac{(1-2M/R)^{1/2}}{(1-2M/r)^{1/2}}\sin\tilde{a}\sin\tilde{b}\right]\sin^3\tilde{a}\sin^2\tilde{b}\,d\tilde{a}\,d\tilde{b}, \quad (25)$$

where $\alpha_0(\tilde{b})$ is the half-angle subtended by the source in the direction $\tilde{b}$.

The Doppler shift of a photon that is seen coming from the direction $(\tilde{a},\tilde{b})$ by an observer at radius r depends on the colatitude where the ray originated, so to evaluate $v^{\hat{\phi}}(\tilde{a},\tilde{b})$ we need to calculate $\theta(\tilde{a},\tilde{b})$. In the Schwarzschild spacetime this leads to elliptical integrals that are best evaluated numerically. Fortunately, the qualitative features introduced by the rotation of the source are also present in Minkowski (flat) spacetime. To provide analytical insight into these features, we therefore simplify here to flat spacetime, and later treat the curved spacetime case numerically. In flat spacetime, for a uniformly rotating source,

$$v^{\hat{\phi}}(\tilde{a}, \tilde{b}) = v_0\left\{1 - \left[\frac{r}{R}\cos\tilde{a} - \left(1 - \frac{r^2}{R^2}\sin^2\tilde{a}\right)^{1/2}\right]^2 \sin^2\tilde{a}\cos^2\tilde{b}\right\}^{1/2}, \quad (26)$$

where v_0 is the locally measured equatorial velocity.

We now consider in turn the following types of sources: a uniformly radiating sphere, a ring of finite width, and an infinitesimal ring. For a sphere,

$$T^{\hat{t}\hat{\phi}} = 4v\frac{r}{R}I_s\frac{\pi}{3}(2 - 3\cos\alpha_0 + \cos^3\alpha_0) \quad (27)$$

and

$$T^{\hat{t}\hat{t}} + T^{\hat{\phi}\hat{\phi}} = I_s\frac{\pi}{3}(8 - 9\cos\alpha_0 + \cos^3\alpha_0), \quad (28)$$

where in flat space $\sin\alpha_0 = R/r$. The average azimuthal velocity

$$v \equiv R\langle\sin\theta\Omega(\theta)\rangle \quad (29)$$

is defined implicitly by equations (24) and (27), where $\Omega(\theta)$ is the angular velocity of the star at colatitude θ and the average is over the emitting surface visible from the test particle. Using equations (18), (27), and (28), we find

$$u_{\phi 0} \to v_0 R \quad \text{as } r \to R, \qquad u_{\phi 0} < v_0 R \quad \text{for } r \gg R. \quad (30)$$

For a radiation source consisting of a thin band around the equator of a sphere of radius R, such that the projected half-thickness of the band is ϵ, numerical integration is necessary. Figure 1*a* shows the equilibrium angular momentum $u_{\phi,0}$ as a function of the height h of the test particle above a slowly rotating band with $v_0 \ll 1$ in flat spacetime, for six values of ϵ ranging from 0.01 to 1.0 (emission from the whole sphere). Note that

$$u_{\phi,0} = \begin{cases} v_0 R, & h \to 0 \text{ and } 0 < \epsilon \le 1; \\ \frac{4}{3}v_0 R, & h \to \infty \text{ and } 0 < \epsilon \ll 1. \end{cases} \quad (31)$$

At large radii the equilibrium angular momentum becomes constant because (see eqs. [18], [27], and [28]) $T^{\hat{t}\hat{\phi}} \sim r\alpha_0^4 a r^{-3}$ as $r \to \infty$ whereas $T^{\hat{t}\hat{t}} + T^{\hat{\phi}\hat{\phi}} \sim \alpha_0^2 \propto r^{-2}$. Thus $u_{\phi,0} = rT^{\hat{t}\hat{\phi}}(T^{\hat{t}\hat{t}} + T^{\hat{\phi}\hat{\phi}})^{-1} \to$ const.

The one-dimensionality of an infinitesimal ring leads to results different from those for a finite ring, even if the finite ring has $\epsilon \ll 1$. For an infinitesimal ring, the locally measured velocity of the radiating matter is always v_0 and the integral is only over $\tilde{a}$ (although it includes a term for $\tilde{b} = \pi/2$ and one for $\tilde{b} = -\pi/2$, which cancel each other for terms in the integrand that are odd functions of $\tilde{b}$). The needed components of the stress-energy tensor are

$$T^{\hat{t}\hat{\phi}} = 2v_0\frac{r}{R}I_s(2\alpha_0 - \sin 2\alpha_0) \quad (32)$$

and

$$T^{\hat{t}\hat{t}} + T^{\hat{\phi}\hat{\phi}} = \tfrac{1}{2}I_s(6\alpha_0 - \sin 2\alpha_0), \quad (33)$$

so that

$$u_{\phi,0} = \begin{cases} \frac{4}{3}v_0 R, & h \to 0; \\ \frac{4}{3}v_0 R, & h \to \infty. \end{cases} \quad (34)$$

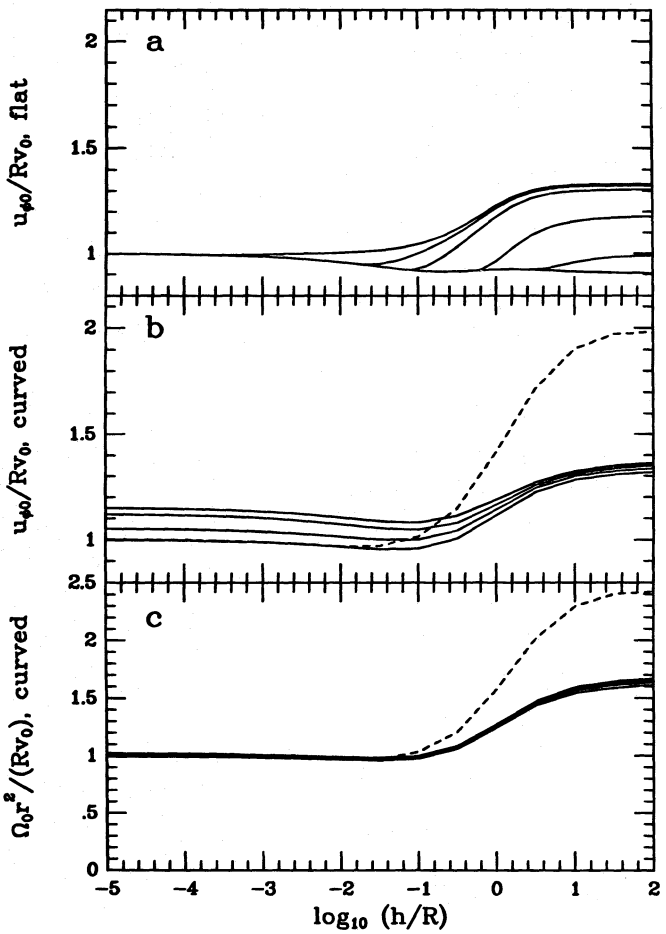

FIG. 1.—Equilibrium angular momentum $u_{\phi 0}$ and velocity Ω_0 as a function of height h above rotating radiation sources of radius R in flat and Schwarzschild spacetimes. (*a*) $u_{\phi 0}$ in units of Rv_0 in flat spacetime for radiation sources with $v_0 \ll 1$. The curves are for equatorial radiation sources with (*top to bottom*) half-widths $\epsilon = 0.01$, 0.1, 0.2, 0.5, 0.8, and 1.0. Near the source $u_{\phi 0}$ is independent of ϵ and equal to Rv_0 whereas far from the source $u_{\phi 0}$ ranges from $0.91Rv_0$ for a spherical source to $(4/3)Rv_0$ for a very thin (but finite) radiating band. (*b*) $u_{\phi 0}$ in units of Rv_0 in Schwarzschild spacetime. The solid curves are for spherical ($\epsilon = 1.0$) radiation sources with $R = 6M$ and (*top to bottom*) $v_0 = 0.5$, 0.4, 0.3, and 0.1. The dashed curve is for an equatorial radiating band with $v_0 = 0.1$ and half-width $\epsilon = 0.1$, and illustrates the increase in $u_{\phi 0}$ at large r that occurs if the radiating region is confined to the rotation equator. At $h \ll R$, $u_{\phi 0}$ is increased by the reduced horizon. At radial infinity, $u_{\phi 0}$ is a factor of 3/2 larger in Schwarzschild spacetime than in flat spacetime because the apparent solid angle subtended by the source is $(1 - 2M/R)^{-1}$ times larger in Schwarzschild spacetime. (*c*) Ω_0 as measured at radial infinity in Schwarzschild spacetime, divided by the angular velocity v_0/R of the radiating matter and multiplied by $(r/R)^2$ to bring out details of the variation. The solid and dashed curves show the same cases as in panel (*b*). At $h \lesssim 10^{-2}R$, Ω_0 is closely equal to the angular velocity of the radiating matter in all these cases.

Thus, the equilibrium angular momentum near an infinitesimal radiating ring differs from that near a very thin but finite ring. Hence, for this (and perhaps other) purposes, rings of finite width cannot be considered to be composed of infinitesimal rings; instead, one must perform two-dimensional computations.

In the Schwarzschild spacetime, ray paths must be determined numerically. The apparent angular extent of the source is greater than it is in flat spacetime; since the equilibrium angular velocity far from a spherical source varies as α_0^2 (see eqs. [18], [27], and [28]), $u_{\phi 0}(\infty)$ in a Schwarzschild spacetime is two factors of the redshift greater than

$u_{\phi 0}(\infty)$ in flat spacetime. Moreover, the smaller horizon increases $u_{\phi 0}$ when $h < R$. The effects of curved spacetime and large velocities are illustrated in Figure 1*b*, which shows how $u_{\phi 0}$ varies with h and v_0 for a test particle orbiting around a uniformly rotating spherical radiation source in a Schwarzschild spacetime, and in Figure 1*c*, which compares the equilibrium angular velocity to the angular velocity of the radiating surface, as measured at infinity.

5. FREE FALL NEAR A ROTATING MASS

To evaluate the effects of radiation forces on particle motion, we must compare particle trajectories in the presence of radiation forces to those in their absence, i.e., to geodesics. Because we are most interested in infall of particles from initially prograde orbits that are close to circular, the geodesics of interest are those followed by particles in equatorial free fall from circular prograde orbits at $R_{\rm ms}$, the radius of the marginally stable orbit. If a particle in such an orbit is perturbed infinitesimally inward, it will fall inward because of gravity alone. We therefore use these geodesic spirals as fiducial motions with which we can compare particle motion in the presence of radiation forces. In this section we first describe our procedure for calculating geodesic particle velocities in an arbitrary stationary, axisymmetric metric. We then focus on the Kerr metric, which allows us to obtain exact analytical expressions for $|j| \leq 1$ with which we can compare our numerical results. Finally, we derive analytical expressions for particle velocities that are valid to first order in j for any arbitrary stationary, axisymmetric metric.

5.1. *General Expressions for Velocities*

To characterize the geodesic motion, we need to know the velocities $v^{\hat{r}}$ and $v^{\hat{\phi}}$ of the particle as seen in the LNRF. If the metric is stationary and axisymmetric but otherwise arbitrary, then

$$v^{\hat{\phi}} \equiv \frac{u^{\hat{\phi}}}{u^{\hat{t}}} = \frac{u_{\hat{\phi}}}{-u_{\hat{t}}} = \frac{e^{\phi}_{\hat{\phi}} u_{\phi}}{-e^{t}_{\hat{t}} u_t - e^{\phi}_{\hat{t}} u_{\phi}} \tag{35}$$

and

$$v^{\hat{r}} \equiv \frac{u^{\hat{r}}}{u^{\hat{t}}} = \frac{e^{r}_{\hat{r}} u_r}{-e^{t}_{\hat{t}} u_t - e^{\phi}_{\hat{t}} u_{\phi}} . \tag{36}$$

Since $u^{\theta} = 0$, $\boldsymbol{u}^2 = -1$ implies

$$u_r^2 = -g_{rr}(1 + g^{tt} u_t^2 + g^{\phi\phi} u_{\phi}^2 + 2 g^{t\phi} u_t u_{\phi}) , \tag{37}$$

so all quantities involved in the calculation of $v^{\hat{\phi}}$ and $v^{\hat{r}}$ can be expressed in terms of the conserved quantities u_{ϕ} and u_t.

In our code, we use equations (35)–(37), the metric and transformation tensors, and the specific angular momentum and specific energy of the particle at the marginally stable orbit to compute the locally measured radial and azimuthal velocities for all radii $r < R_{\rm ms}$.

5.2. *Geodesics in the Kerr Metric*

Exact, analytical results are available for the radial and azimuthal velocities of particles in free fall in Kerr spacetime for $0 \leq j \leq 1$. We can therefore test our numerical code by comparing the results it gives with these exact results.

In the Kerr metric, the radius of the marginally stable prograde equatorial orbit is (Bardeen et al. 1972)

$$R_{\rm ms} = M\{3 + Z_2 - [(3 - Z_1)(3 + Z_1 + 2Z_2)]^{1/2}\} , \tag{38a}$$

where

$$Z_1 \equiv 1 + (1 - j^2)^{1/3}[(1 + j)^{1/3} + (1 - j)^{1/3}] \tag{39a}$$

and

$$Z_2 \equiv (3j^2 + Z_1^2)^{1/2} . \tag{39b}$$

The specific angular momentum and energy of a particle in a prograde circular orbit at radius r outside the radius $r_{\rm ph} = 2M\{1 + \cos[\frac{2}{3}\cos^{-1}(-j)]\}$ of the photon orbit are

$$u_{\phi} = \frac{(Mr)^{1/2}[r^2 - 2jM(Mr)^{1/2} + j^2M^2]}{r[r^2 - 3Mr + 2jM(Mr)^{1/2}]^{1/2}} \tag{40}$$

and

$$-u_t = \frac{r^2 - 2Mr + jM(Mr)^{1/2}}{r[r^2 - 3Mr + 2jM(Mr)^{1/2}]^{1/2}} . \tag{41}$$

Table 2 compares the results given by expressions (40) and (41) with the numerical results given by our code for the proper radial and azimuthal velocities of a particle falling freely inward from the marginally stable circular orbit, for 10 values of j ranging from 0 to 0.9. Both the analytical and numerical velocities are computed to all orders in j. All entries start at $R_{\rm ms}$, and comparisons are made at $(R_{\rm ms} - r)/(R_{\rm ms} - r_+)$ equal to 0, 0.2, 0.4, 0.6, and 0.8, where $r_+ = M(1 - j^2)^{1/2}$ is the radius of the horizon. The results listed in Table 2 were generated using a grid spacing that becomes finer close to the horizon, like the grid we use in our calculations of particle orbits with radiation drag around neutron stars. At $(R_{\rm ms} - r)/(R_{\rm ms} - r_+) = 0.8$, the numerical and analytical velocities differ by at most 0.3%. As expected, the percentage differences between the analytical and numerical results for the radial velocity are larger near $R_{\rm ms}$, where the radial velocity is small, whereas the analytical and numerical results for the azimuthal velocity agree well everywhere.

5.3. *First-Order Expressions*

The results just obtained for the Kerr spacetime cannot be applied to rapidly rotating relativistic stars because the spacetime around them deviates significantly from Kerr (see Friedman et al. 1986; Cook et al. 1994). In contrast, the spacetime around any slowly rotating gravitating mass (that is, one with $j \ll 1$), whether a star or black hole, depends only on M and j and is therefore independent of the nature of the gravitating mass (Hartle & Thorne 1968). Hence, by expanding equations (40) and (41) to first order in j and solving them explicitly, we can obtain expressions for the azimuthal and radial velocity of a particle falling onto any slowly rotating star or black hole valid to this order.

To first order in j,

$$R_{\rm ms} \approx 6M[1 - (\tfrac{2}{3})^{3/2} j] , \tag{42}$$

$$u_{\phi,\rm ms} \approx \sqrt{12}\, M[1 - \tfrac{1}{2}(\tfrac{2}{3})^{3/2} j] , \tag{43}$$

and

$$u_{t,\rm ms} \approx -\sqrt{\tfrac{8}{9}}[1 - \tfrac{1}{16}(\tfrac{2}{3})^{3/2} j] . \tag{44}$$

Hence, for a particle that is initially in a circular orbit at $R_{\rm ms}$ and is then displaced infinitesimally inward, the velocity components measured in the LNRF at $r < R_{\rm ms}$ are

TABLE 2

FREE-FALL VELOCITIES

r/M	$v_a^{\hat{\phi}}$	$v_n^{\hat{\phi}}$	$v_a^{\hat{r}}$	$v_n^{\hat{r}}$
$j = 0$, $R_{ms} = 6.0M$, $u_{\phi,ms} = 3.464M$				
6.000.....	0.500	0.500	0	0
5.200.....	0.554	0.555	−0.021	−0.022
4.400.....	0.617	0.617	−0.078	−0.078
3.600.....	0.680	0.681	−0.192	−0.192
2.800.....	0.701	0.702	−0.432	−0.433
$j = 0.1$, $R_{ms} = 5.669M$, $u_{\phi,ms} = 3.367M$				
5.669.....	0.511	0.511	0	0
4.934.....	0.563	0.564	−0.021	−0.022
4.200.....	0.624	0.624	−0.076	−0.076
3.465.....	0.684	0.685	−0.188	−0.188
2.730.....	0.704	0.704	−0.422	−0.422
$j = 0.2$, $R_{ms} = 5.329M$, $u_{\phi,ms} = 3.264M$				
5.329.....	0.522	0.522	0	0
4.660.....	0.573	0.573	−0.021	−0.023
3.990.....	0.631	0.631	−0.075	−0.075
3.320.....	0.688	0.688	−0.185	−0.185
2.650.....	0.706	0.706	−0.413	−0.413
$j = 0.3$, $R_{ms} = 4.979M$, $u_{\phi,ms} = 3.154M$				
4.979.....	0.534	0.534	0	0
4.374.....	0.583	0.584	−0.021	−0.022
3.769.....	0.638	0.638	−0.074	−0.074
3.164.....	0.692	0.692	−0.181	−0.181
2.559.....	0.706	0.707	−0.405	−0.405
$j = 0.4$, $R_{ms} = 4.164M$, $u_{\phi,ms} = 3.034M$				
4.614.....	0.547	0.547	0	0
4.075.....	0.594	0.594	−0.020	−0.022
3.535.....	0.646	0.646	−0.073	−0.073
2.996.....	0.695	0.695	−0.178	−0.178
2.456.....	0.706	0.707	−0.398	−0.398
$j = 0.5$, $R_{ms} = 4.233M$, $u_{\phi,ms} = 2.903M$				
4.233.....	0.562	0.562	0	0
3.760.....	0.606	0.606	−0.020	−0.021
3.286.....	0.654	0.654	−0.072	−0.072
2.813.....	0.698	0.698	−0.175	−0.174
2.339.....	0.705	0.705	−0.391	−0.391
$j = 0.6$, $R_{ms} = 3.829M$, $u_{\phi,ms} = 2.756M$				
3.829.....	0.577	0.577	0	0
3.423.....	0.618	0.618	−0.020	−0.022
3.017.....	0.661	0.661	−0.071	−0.072
2.612.....	0.700	0.700	−0.172	−0.172
2.206.....	0.701	0.701	−0.386	−0.386
$j = 0.7$, $R_{ms} = 3.393M$, $u_{\phi,ms} = 2.586M$				
3.393.....	0.594	0.594	0	0
3.057.....	0.630	0.630	−0.020	=0.023
2.722.....	0.667	0.667	−0.070	−0.072
2.386.....	0.699	0.699	−0.170	−0.170
2.050.....	0.694	0.694	−0.382	−0.382
$j = 0.8$, $R_{ms} = 2.907M$, $u_{\phi,ms} = 2.380M$				
2.907.....	0.611	0.611	0	0
2.645.....	0.641	0.641	−0.020	−0.021
2.384.....	0.671	0.671	−0.069	−0.070
2.123.....	0.695	0.695	−0.168	−0.168
1.861.....	0.681	0.681	−0.380	−0.380
$j = 0.9$, $R_{ms} = 2.321M$, $u_{\phi,ms} = 2.100M$				
2.321.....	0.625	0.625	0	0
2.144.....	0.646	0.645	−0.020	−0.023
1.967.....	0.665	0.665	−0.069	−0.071
1.790.....	0.676	0.677	−0.168	−0.169
1.613.....	0.653	0.653	−0.381	−0.382

NOTE.—Comparison of the numerical and analytical estimates for the radial velocity $v^{\hat{r}}$ and azimuthal velocity $v^{\hat{\phi}}$ (as measured in the LNRF at the particle) for test particles in equatorial free fall from the marginally stable orbit, for $0 \le j \le 0.9$. For each value of j, we list the Boyer-Lindquist radius R_{ms} of the marginally stable orbit and the specific angular momentum $u_{\phi,ms}$ of a particle in a circular orbit at R_{ms}. We then compare the numerical (denoted by the subscript n) and analytical (denoted by the subscript a) estimates for the radial and azimuthal velocities at radii r such that $(R_{ms} - r)/(R_{ms} - r_+) = 0$, 0.2, 0.4, 0.6, and 0.8, where $r_+ = M + M(1 - j^2)^{1/2}$ is the Boyer-Lindquist radius of the horizon. The numerical and analytical estimates are in excellent agreement, with a maximum deviation of $\sim 0.3\%$ at $(R_{ms} - r)/(R_{ms} - r_+) = 0.8$. As expected, $v_n^{\hat{r}}$ differs most from $v_a^{\hat{r}}$ when $v^{\hat{r}}$ is small, near R_{ms}, whereas the estimates for $v^{\hat{\phi}}$ agree everywhere to high precision.

$$v^{\hat{\phi}} = \left(\frac{27}{2}\right)^{1/2} \frac{(1 - 2M/r)^{1/2}}{r/M} \left[1 - \left(\frac{7}{16} - \frac{27}{2(r/M)^3}\right)\left(\frac{2}{3}\right)^{3/2} j\right] \tag{45}$$

and

$$v^{\hat{r}} = \left(\frac{6 - r/M}{2r/M}\right)^{3/2} \times \left[1 + \left(\frac{1}{8} + \frac{27}{(r/M)^3} - \frac{12 + r/M}{6 - r/M}\right)\left(\frac{2}{3}\right)^{3/2} j\right]^{1/2} . \tag{46}$$

The corresponding components in the static frame are

$$w^{\hat{\phi}} = \left(\frac{27}{2}\right)^{1/2} \frac{(1 - 2M/r)^{1/2}}{r/M} \left[1 - \left(\frac{7}{16} - \frac{1}{r/M - 2}\right)\left(\frac{2}{3}\right)^{3/2} j\right] \tag{47}$$

and

$$w^{\hat{r}} = \left(\frac{6 - r/M}{2r/M}\right)^{3/2} \left[1 + \left(\frac{1}{8} - \frac{12 + r/M}{6 - r/M}\right)\left(\frac{2}{3}\right)^{3/2} j\right]^{1/2} . \tag{48}$$

Thus, at R_{ms},

$$v^{\hat{\phi}} = \tfrac{1}{2}[1 + \tfrac{3}{8}(\tfrac{2}{3})^{3/2} j] \tag{49}$$

and

$$w^{\hat{\phi}} = \tfrac{1}{2}[1 + \tfrac{9}{16}(\tfrac{2}{3})^{3/2} j] . \tag{50}$$

Expressions (45) and (47) for the azimuthal velocity are accurate to first order in j for any $r \le R_{ms}$. In contrast, expressions (46) and (48) for the radial velocity are accurate only if $6 - r/M \gg j$. For example, if one expands the exact expressions for the velocity components in the Kerr metric to higher order in j, one finds terms of order $j^2/(6M - r)^2$ and $j^3/(6M - r)^3$, which are comparable to or larger than the $\mathcal{O}(j)$ term when $6 - r/M \lesssim j$. The error made by neglecting these terms is obviously large for $r = R_{ms}$. For example, at R_{ms} expression (46) erroneously predicts $v^{\hat{r}} = (-2)^{1/2}[(\frac{2}{3})^{3/2} j/2]^{3/2}$ instead of 0. This seems not to have been noticed by Kluzniak & Wagoner (1985), who give an

expression for $v^{\hat{\phi}}$ near but inside $R_{\rm ms}$ that becomes imaginary very close to $R_{\rm ms}$.

Another subtlety enters in the choice of the orthonormal tetrad in which one makes velocity measurements. To first order in j, the off-diagonal components of the transformation tensor from Boyer-Lindquist coordinates to the LNRF are

$$e_{\hat{t}}^{\phi} = \frac{2jM^2}{r^3(1-2M/r)^{1/2}}, \quad e_{\hat{\phi}}^{t} = 0. \tag{51}$$

More generally, one can define a family of reference frames related to the Boyer-Lindquist coordinate system by the transformation with off-diagonal components

$$e_{\hat{t}}^{\phi} = \frac{2jM^2\lambda}{r^3(1-2M/r)^{1/2}}, \quad e_{\hat{\phi}}^{t} = -\frac{2jM^2(1-\lambda)}{r^3(1-2M/r)}, \tag{52}$$

where λ is a nondimensional parameter that fixes the azimuthal velocity of the frame relative to the static frame, in units of the azimuthal velocity of the LNRF as seen from infinity (if $\lambda = 0$, the frame is at rest as seen from infinity). All of these frames are orthonormal to first order in j; however, only the LNRF ($\lambda = 1$) is orthonormal to all orders. Obviously, the choice of λ affects the inferred azimuthal velocity of accreting particles. Kluzniak & Wagoner (1985) use the frame that corresponds to $\lambda = 1/2$, and find a first-order azimuthal velocity $v^{\hat{\phi}} = (1/2)[1 + (15/32)(2/3)^{3/2}j]$. This overestimates slightly the angle at which a particle accreting onto a neutron star hits the stellar surface, as seen by a static observer, since the angle should instead be calculated using expression (50).

6. RADIATION FIELD AROUND A SLOWLY ROTATING MASS AND RADIATION SOURCE

The frequency shift from the stellar surface to the LNRF at the radial position r of the test particle is just the Doppler shift from the frame comoving with the stellar surface to the LNRF there, plus the shift from the LNRF at the stellar surface to the LNRF at r. We use the subscript e to denote the value of a quantity measured by a comoving observer at the emitting surface, the subscript l for the value of the same quantity measured by an observer in the LNRF at the emitting surface, and the subscript r for the value of the same quantity measured by an observer in the LNRF at the position of the test particle.

The frequency of the radiation in the LNRF at the emitting surface is given by the Doppler relation

$$\nu_l = \frac{\nu_e}{\gamma(1 - v^{\hat{\phi}}\cos\psi)}, \tag{53}$$

where $v^{\hat{\phi}}$ is the velocity of the emitting surface, ψ is the angle between $\boldsymbol{v}$ and the ray path as measured in the LNRF, and $\gamma \equiv (1 - [v^{\hat{\phi}}]^2)^{-1/2}$. The frequency in the LNRF at the test particle is

$$\nu_r = \left[\frac{e^{f_e}(1 + \omega_e u_\phi/u_t)^{-1}}{e^{f_r}(1 + \omega_r u_\phi/u_t)^{-1}}\right]\nu_l, \tag{54}$$

where $e^{2f} = -g_{tt}$.

In our numerical code we calculate the frequency shifts exactly, but for analytical purposes we now compute the first-order effects of the rotation of the gravitating mass on the needed components of the radiation stress-energy tensor. The first task is to determine the angular extent of the star as seen at the test particle. If the stellar radius R is greater than the radius $r_{\rm ph}$ of the photon orbit, then the limb of the star corresponds to photons leaving the stellar surface at a grazing angle. This gives the relation (see Bardeen et al. 1972)

$$V_r(R) = 0, \tag{55}$$

where, for the Kerr metric, the effective radial potential is

$$V_r(r) = [u_t(r^2 + j^2M^2) + jMu_\phi]^2 - (r^2 - 2Mr + j^2M^2)[(u_\phi + jMu_t)^2 + q]. \tag{56}$$

Here $q \equiv u_\theta^2 + \cot^2\theta u_\phi^2 - j^2M^2\cos^2\theta u_t^2$ is Carter's fourth constant of motion; θ is the colatitude of the particle. Transforming from Boyer-Lindquist coordinates to the LNRF at r and using the definitions of $\tilde{a}$ and $\tilde{b}$, we find that to first order in j the extent α of the limb in the angle $\tilde{a}$ is given as a function of $\tilde{b}$ by

$$\sin\alpha = \frac{R}{r}\frac{(1-2M/r)^{1/2}}{(1-2M/R)^{1/2}} \times\left[1 - 2j\frac{M^2(1-R^3/r^3)}{R^2(1-2M/R)^{1/2}}\sin\theta\sin\tilde{b}\right] \equiv \sin\alpha_0\left[1 - 2j\frac{M^2(1-R^3/r^3)}{R^2(1-2M/R)^{1/2}}\sin\theta\sin\tilde{b}\right]. \tag{57}$$

Thus, an observer at rest in the LNRF at radius r sees frame-dragging that increases the apparent extent of the backward limb while diminishing the apparent extent of the forward limb by the same amount.

Consider next the Doppler shift caused by the rotation of the radiation source. The magnitude of the shift of a photon that is seen coming from the direction $(\tilde{a}, \tilde{b})$ depends on the velocity $v^{\hat{\phi}}(\tilde{a}, \tilde{b})$ of the emitting surface at the point where it originated. To first order in $v^{\hat{\phi}}$, the frequency of the photon as seen in the LNRF at the emitting surface is

$$\nu_l = \left[1 + v^{\hat{\phi}}\frac{(1-2M/R)^{1/2}}{(1-2M/r)^{1/2}}\sin\tilde{a}\sin\tilde{b}\right]\nu_e. \tag{58}$$

The next task is to calculate the frequency shift from the LNRF at the emitting surface to the LNRF at r. To first order in j, the frequency in the LNRF at r is

$$\nu_r = \frac{(1-2M/R)^{1/2}}{(1-2M/r)^{1/2}}\left[1 + 2j\left(\frac{M^3}{R^3} - \frac{M^3}{r^3}\right) \times\frac{r/M}{(1-2M/r)^{1/2}}\sin\tilde{a}\sin\tilde{b}\right]\nu_l. \tag{59}$$

There are no factors involving the colatitude of the observer, because to first order in j the angular frequency of the LNRF depends only on r, not θ. Combining equations (58) and (59), we obtain the relation

$$\nu_r \approx \frac{(1-2M/R)^{1/2}}{(1-2M/r)^{1/2}}\left\{1 + \frac{r/M}{(1-2M/r)^{1/2}}\left[2j\left(\frac{M^3}{R^3} - \frac{M^3}{r^3}\right) + v^{\hat{\phi}}(\tilde{a}, \tilde{b})\frac{(1-2M/R)^{1/2}}{r/M}\right]\sin\tilde{a}\sin\tilde{b}\right\}\nu_e, \tag{60}$$

which is valid to first order in j and $v^{\hat{\phi}}$.

We now specialize to particles in the equatorial plane, i.e., $\theta = \pi/2$. For such particles, comparison of the relative sizes of the j and v^{ϕ} terms in equation (60) shows that the Doppler shift is typically much more important than the

change in the frequency of the LNRF with radius: if $R > 4M$ and the radiating surface moves with the gravitating mass then the change in the LNRF frequency is at most $\sim 15\%$ of the Doppler shift. That this is not accidental can be seen by considering the relative angular frequencies of the LNRF and star at the stellar surface. For example, for a sphere of uniform density spinning with angular frequency $\Omega = (5/2)jM/R^2$, the LNRF frequency is, to first order, $\omega = 2jM^2/R^3$ and hence $\omega/\Omega = 0.8M/R$. Thus, for most neutron stars, $\omega/\Omega < 0.2$. This means that the effects of frame-dragging are generally small compared to the effects of Doppler shifts. Therefore, for a slowly rotating mass and radiation source, the expression for the frequency shift can be simplifed by including only special relativistic terms and ignoring frame dragging. In this approximation, the specific intensity observed in the equatorial plane in the local direction $\tilde{a}, \tilde{b}$ is given by equation (22).

We can now compute the needed components of the radiation stress-energy tensor. In general $v^{\hat{\phi}}(\tilde{a}, \tilde{b})$ depends on the colatitude $\theta(R)$ of the ray at the radiating surface, so $\theta(R)$ must be calculated for each $\tilde{a}$ and $\tilde{b}$. Unfortunately, $\theta(R)$ does not follow straightforwardly from conserved quantities such as u_ϕ, so that ray tracing is required. To see this, consider a photon propagating in the Schwarzschild spacetime that arrives at an equatorial observer with $u_\phi = u_\theta = 0$. Clearly, the photon had to originate from the stellar equator. But since a radially directed photon emitted from anywhere on the stellar surface has the same four-momentum as this photon, the four-momentum does not specify the initial θ or ϕ. The same is true when j is not zero. From Bardeen et al. (1972), the equation to be solved is

$$\frac{d\theta}{dr} = \pm \frac{(q - u_\phi^2 \cot^2 \theta/u_t^2)^{1/2}}{V_r(r)^{1/2}} . \tag{61}$$

The solution of equation (61) is an elliptical integral that does not give much insight into the problem. To make further analytical progress we define (compare eq. [29])

$$v \equiv R\langle \sin \theta[\Omega(\theta) - \omega]\rangle . \tag{62}$$

Here $\Omega(\theta)$ is the angular velocity of the star at colatitude θ and ω is the angular velocity of the LNRF at the stellar surface, as measured by a static observer at radius R and colatitude θ; $d\omega/d\theta$ is $\mathcal{O}(j^3)$, so the dependence of ω on colatitude can be neglected. The average denoted by the brackets is over the emitting surface visible from the test particle.

Using expressions (57) and (22), we find (see Appendix B) that the radial energy flux and the diagonal components of the stress-energy tensor are unaffected to first order in the rotation rates of the gravitating mass and radiation source. The off-diagonal components are

$$T^{\hat{t}\hat{\phi}} \approx \frac{4}{3}\pi I_0(r) \frac{v}{\sin \alpha_0}(\cos^3 \alpha_0 - 3 \cos \alpha_0 + 2)$$

$$\sim \pi v I_s \left(1 - \frac{2M}{R}\right)^{1/2} \left(\frac{R}{r}\right)^3 \quad \text{as } r \to \infty \tag{63}$$

$$T^{\hat{r}\hat{\phi}} \approx \pi I_0(r) v \sin^3 \alpha_0$$

$$\sim \pi v I_s \left(1 - \frac{2M}{R}\right)^{1/2} \left(\frac{R}{r}\right)^3 \quad \text{as } r \to 0 , \tag{64}$$

where $I_0(r) \equiv I_s(1 - 2M/R)^2/(1 - 2M/r)^2$ is the specific intensity at the particle in a Schwarzschild spacetime (see, e.g., AEL) and we have assumed that the frequency-integrated specific intensity I_s seen by an observer comoving with the stellar surface is isotropic and independent of the location on the surface.

7. PARTICLE ORBITS AROUND A SLOWLY ROTATING MASS AND RADIATION SOURCE

Using the formalism developed in §§ 2 and 6 and the numerical method described in § 2, we have followed the inspiral of accreting particles acted on by radiation forces. To examine the effects of nonuniform emission as well as the effects of rotation of the gravitating mass and the radiation source, we computed the stress-energy tensor of the radiation produced by sources with equatorial radii of $4M$, widths ϵ of 1.0, 0.5, and 0.1 (ϵ was defined in § 4), and gravitating masses with $j = 0$, 0.1, 0.2, and 0.3. For simplicity, the computations were carried out in the Kerr spacetime because, as noted above, photon and particle trajectories in this spacetime are the same to first order as in any stationary axisymmetric spacetime. However, we emphasize again that to higher order in j the exterior spacetime of rotating stars deviates from the Kerr geometry.

In ML93 we assumed isotropic emission by a spherically symmetric star in the Schwarzschild spacetime. For that investigation it was convenient to parameterize the luminosity using the ratio of the total luminosity at infinity L^∞ to the Eddington critical luminosity at infinity L_E^∞, which is the luminosity at which the radial component of the radiation force on a static particle at infinity exactly balances gravity. In the present paper the anisotropic emission patterns we consider make the total luminosity a less useful quantity. Instead we define a critical specific intensity I_E at the star such that the radiation force on a static particle in the equatorial plane at infinity exactly balances gravity, and use $i \equiv I(R)/I_E$ to characterize the intensity of the radiation at the source. For $\epsilon = 1.0$ and $j = 0$ (the case treated in ML93), this definition reduces to the previous one.

The initial angular momentum of the test particle was chosen to be that of a particle in a circular orbit, so that for $u^r = u^\theta = 0$, $du^r/d\tau = 0$ at its initial radius $r = 9M$. We solved for the initial value of u_ϕ to first order in j using the radial force equation

$$a^r = -\frac{\sigma}{m} T^{tr} u_t . \tag{65}$$

If $du^r/d\tau = 0$, then to first order in j,

$$a^r = \frac{M}{r^2} - \left(1 - \frac{3M}{r}\right)\frac{u_\phi^2}{r^3} + \frac{6jM^2 u_\phi u_t}{r^4} . \tag{66}$$

The radiation flux T^{tr} was computed numerically. We chose an initial radial velocity of 1% of the initial azimuthal velocity, to simulate the effect of a small viscosity in an accretion disk. As was also true for the results reported in ML93, the choice of the initial radial velocity has little effect on the results reported here, so that choosing initial values of $v^{\hat{r}}/v^{\hat{\phi}}$ of 10^{-3} or 10^{-1} would yield essentially the same velocity curves and the same final specific energy and angular momentum.

Table 3 lists selected results for the initial and final specific energies and angular momenta of particles that start in a circular orbit at $9M$ and eventually accrete onto a star of radius $4M$. Displayed are the initial and final specific

TABLE 3

INITIAL AND FINAL ENERGY AND ANGULAR MOMENTUM

$I(R)/I_E$	ϵ	j	$u_{\phi,i}$	$u_{\phi,f}$	$u_{\phi,R}$	e_i	e_f	Δe_B
0.05.....	1.0	0	3.56	2.66	0	0.9484	0.8787	0.1716
		0.1	3.51	2.67	0.284	0.9476	0.8817	0.1719
		0.2	3.47	2.67	0.574	0.9471	0.8837	0.1654
		0.3	3.42	2.66	0.878	0.9462	0.8854	0.1524
	0.5	0	3.60	2.73	0	0.9499	0.8808	0.1737
		0.1	3.55	2.72	0.284	0.9490	0.8826	0.1727
		0.2	3.50	2.70	0.574	0.9482	0.8833	0.1650
		0.3	3.46	2.66	0.878	0.9477	0.8843	0.1510
	0.1	0	3.66	3.02	0	0.9521	0.9004	0.1933
		0.1	3.61	2.97	0.284	0.9512	0.9002	0.1903
		0.2	3.56	2.90	0.574	0.9504	0.8990	0.1807
		0.3	3.52	2.84	0.878	0.9496	0.8979	0.1649
0.2.....	1.0	0	3.20	1.43	0	0.9360	0.7899	0.0818
		0.1	3.16	1.55	0.284	0.9356	0.7970	0.0871
		0.2	3.11	1.65	0.574	0.9348	0.8040	0.0857
		0.3	3.06	1.78	0.878	0.9340	0.8134	0.0804
	0.5	0	3.37	1.62	0	0.9417	0.7948	0.0877
		0.1	3.32	1.71	0.284	0.9409	0.8018	0.0919
		0.2	3.27	1.80	0.574	0.9401	0.8085	0.0902
		0.3	3.23	1.90	0.878	0.9396	0.8171	0.0841
	0.1	0	3.60	2.33	0	0.9499	0.8348	0.1277
		0.1	3.55	2.33	0.284	0.9490	0.8384	0.1285
		0.2	3.51	2.32	0.574	0.9485	0.8409	0.1226
		0.3	3.46	2.32	0.878	0.9477	0.8450	0.1120
0.5.....	1.0	0	2.35	0.24	0	0.9117	0.7186	0.0115
		0.1	2.32	0.47	0.284	0.9114	0.7228	0.0129
		0.2	2.28	0.70	0.574	0.9110	0.7297	0.0114
		0.3	2.23	0.95	0.878	0.9104	0.7413	0.0083
	0.5	0	2.86	0.51	0	0.9254	0.7211	0.0140
		0.1	2.82	0.63	0.284	0.9250	0.7262	0.0163
		0.2	2.77	0.82	0.574	0.9242	0.7333	0.0150
		0.3	2.73	1.04	0.878	0.9238	0.7446	0.0116
	0.1	0	3.49	1.42	0	0.9459	0.7612	0.0541
		0.1	3.44	1.50	0.284	0.9451	0.7671	0.0572
		0.2	3.40	1.54	0.574	0.9446	0.7719	0.0536
		0.3	3.35	1.56	0.878	0.9438	0.7758	0.0428

NOTE.—Initial and final angular momentum and energy of test particles in initially circular orbits around radiating stars in a Kerr spacetime. Here the particle is initially at a Boyer-Lindquist radius of $9M$, the star has a Boyer-Lindquist radius of $R = 4M$, and the radiating surface is assumed to rotate with the gravitating mass. The radiation comes from a band on the surface with half-width ϵR, and the specific intensity $I(R)$ at the surface (assumed to be uniform over the band and isotropic in the outward direction) is $I(R)/I_E = 0.05$, 0.2, or 0.5, where I_E is the specific intensity such that the radial radiation force at infinity in the equatorial plane is equal to the gravitational force at infinity. For a given $I(R)/I_E$, ϵ, and j, Table 3 lists the initial specific angular momentum $u_{\phi,i}$, the specific angular momentum $u_{\phi,f}$ just before impact, the specific angular momentum $u_{\phi,R}$ of a particle moving with the stellar surface at the equator, the initial specific energy e_i, the specific energy e_f just before impact, and the difference Δe_B between e_f and the specific energy of a particle moving with the star at the equator. Thus, Δe_B is a measure of the amount of energy released in a boundary layer at the stellar surface. Typically, rotation decreases the effects of radiation drag, but (as discussed in the text) for very small radiation energy densities the increased inspiral time for higher j more than compensates for the decreased loss rates of energy and angular momentum, and *more* energy and angular momentum can be transferred to the radiation field for higher j.

angular momenta $u_{\phi,i}$ and $u_{\phi,f}$ and the initial and final specific energies e_i and e_f, for various combinations of i, ϵ, and j. In this case the "final" values are those of the particle just before impact. Also listed are $u_{\phi,R}$, the specific angular momentum of a particle moving with the stellar surface at the equator, and Δe_B, the difference between the specific energy of a particle just prior to impact and the specific energy of a particle moving with the stellar surface. Thus Δe_B is a measure of how much energy is liberated in a boundary layer at the surface.

The introduction of rotation produces two competing effects. First, because the resulting radiation field has nonzero angular momentum, the energy and angular momentum loss rates are decreased for prograde orbits. Second, both the change in the spacetime caused by the rotation of the gravitating mass and the radial component of the radiation force increase the inspiral time compared to the inspiral time for a particle near a nonrotating nonluminous star. Since the total loss is the integral of the loss rate over time, which effect wins depends on the values of i, ϵ, and j.

The overall behavior is fairly complex, but some general trends are evident. The increase in the inspiral time appears to be more important for lower radiation energy densities (that is, for low i and/or low ϵ), whereas the decrease in the loss rate dominates for higher radiation energy densities. For a given i and ϵ, the final specific energy generally increases with increasing j, even though the initial specific energy decreases with increasing j. Thus the amount of energy transferred from the particle to the radiation field generally *decreases* with increasing j (of course, in the test particle approximation the change in the radiation field is neglected). The exception occurs when $i = 0.05$ and $\epsilon = 0.1$, because the radiation energy density is very small and the energy transferred to the radiation field is approximately independent of j. Similarly, only when $i = 0.05$ and $\epsilon = 0.1$ is more angular momentum transferred to the radiation field for higher j. Only for very small radiation energy densities is the increase in inspiral time more important than the decrease in loss rate. However, for any given value of i, $u_{\phi,f}(j = 0.3) - u_{\phi,f}(j = 0)$ decreases with decreasing ϵ. The same trend holds for the final energy e_f. We also see that for any intensity or width of the emitting region, Δe_B decreases with increasing j for $j \geq 0.1$, showing the growing importance of increased inspiral time as the radiation energy density decreases.

Figures 2, 3, and 4 show the radial and azimuthal velocity components of an inspiraling particle as a function of radius, as measured by an observer in the LNRF, for $\epsilon = 0.1$, 0.5, and 1.0, and several representative combinations of i and j. For a given j, the mean azimuthal velocity decreases with increasing radiation flux, both because the initial azimuthal velocity for a circular orbit is smaller for larger flux and because more angular momentum is removed at a given radius. Thus, for specified j and i, $dv^{\hat{\phi}}/d\epsilon < 0$ and for specified j and ϵ, $dv^{\hat{\phi}}/dI(R) < 0$.

The radial velocity does not show such simple trends. For any j and for $i = 0.05$ or 0.2, the radial velocity shortly after the initial infall satisfies $dv^{\hat{r}}/d\epsilon > 0$. The reason is that for low to intermediate fluxes, the more angular momentum is removed from the particle the less centrifugal support there is against gravity, and the greater is the particle's inward velocity. However, for $i = 0.5$, the radial flux is so high that for particles with significant radial velocities near the star, the flux seen in the inertial frame momentarily comoving with the particle exceeds the Eddington critical flux, causing the radial velocity to decrease. This leads to complicated crossover behavior, in which the radial velocity for $\epsilon = 0.1$ starts out small and increases more rapidly than for $\epsilon = 0.5$ or 1.0 but then reaches a peak, and finally decreases rapidly as the distance from the star becomes less than ϵR.

The trends of the radial velocity with j emphasize the importance of centrifugal support and of the previously mentioned competition between decreased angular momen-

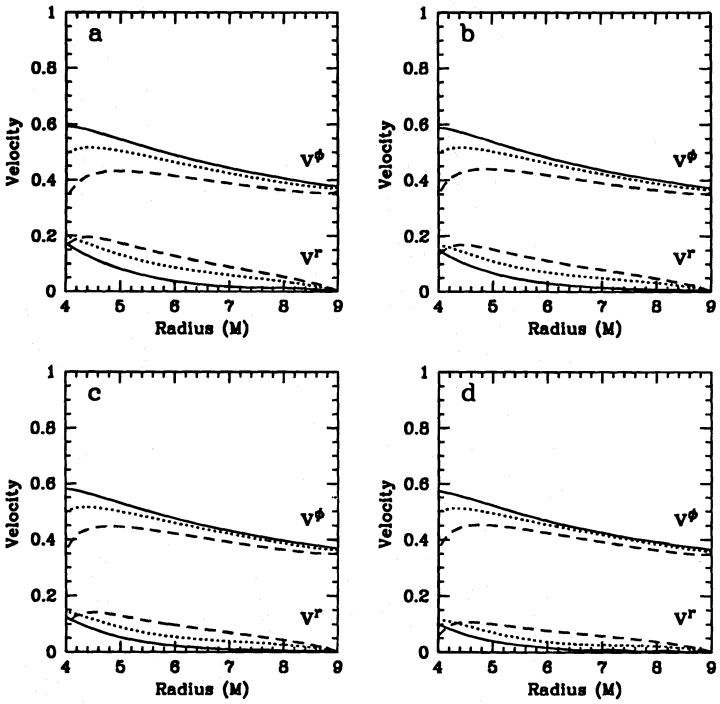

FIG. 2.—Locally measured radial and azimuthal velocity components $v^{\hat{\phi}}$ and $v^{\hat{r}}$ (in units of c) as functions of radius for particles spiraling inward from $r = 9M$ to the surface of a star with radius $R = 4M$ and an equatorial emission region of half-width $\epsilon = 0.1$. Panels (*a*)–(*d*) display velocity profiles for stars with angular momenta $j = 0$, 0.1, 0.2, and 0.3, respectively. Shown in each panel are profiles for $i = 0.05$ (*solid curve*), $i = 0.2$ (*dotted curve*), and $i = 0.5$ (*dashed curve*), where i is the intensity at the surface of the star $I(R)$ in units of the critical surface intensity I_E such that the radiation force on a static particle in the equatorial plane at infinity would exactly balance gravity (see text).

tum and energy loss rates and increased inspiral time. For all values of i and ϵ, $dv^{\hat{r}}/dj < 0$, because the frame-dragging caused by a rotating gravitating mass provides radial support for the particle. For azimuthal velocities we find that, if i and ϵ are both small (so that the flux is low), then $dv^{\hat{\phi}}/dj < 0$, whereas if the flux is relatively high then $dv^{\hat{\phi}}/dj > 0$. This is consistent with our findings concerning the final energy and angular momentum. Thus again the

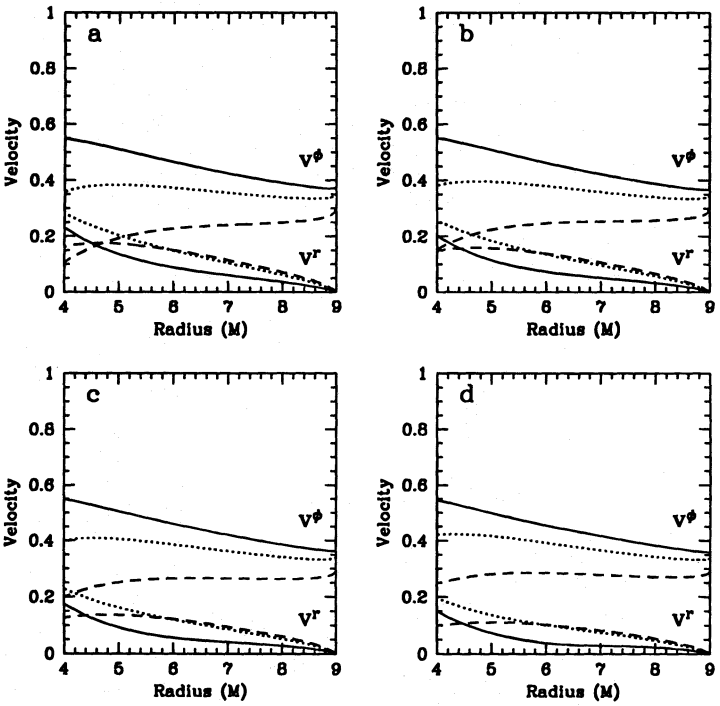

FIG. 3.—Locally measured radial and azimuthal velocity components ($v^{\hat{\phi}}$ and $v^{\hat{r}}$ in units of c) as functions of radius for the same conditions as in Fig. 2, except $\epsilon = 0.5$.

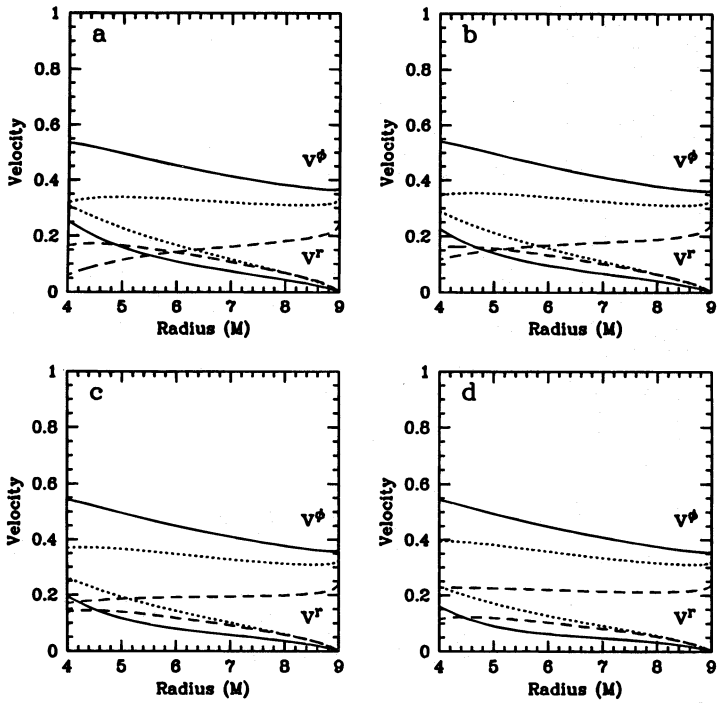

FIG. 4.—Locally measured radial and azimuthal velocity components ($v^{\hat{\phi}}$ and $v^{\hat{r}}$ in units of c) as functions of radius for the same conditions as in Fig. 2, except $\epsilon = 1.0$.

increased inspiral time is more important for lower fluxes whereas the decreased angular momentum loss rate is more important for higher fluxes.

8. SUMMARY AND DISCUSSION

In this section we first summarize briefly our results for test particle motion around slowly rotating sources and gravitating masses and discuss the conditions under which our results for test particles are applicable to accreting fluid flows. We then consider the specific effects of radiation forces on accretion flows near X-ray burst sources during a burst and flows near accretion-powered neutron stars; in both cases we analyze the differences between geometrically thick and geometrically thin flows. Finally, we discuss the effects of radiation forces on the long-term spin up of accreting neutron stars. For definiteness, we assume that radiation interacts with accreting matter only via scattering, that the star accretes matter via an accretion disk, and that the disk is optically thin in the vertical direction. We defer treatment of optically thick flows to a future paper.

8.1. *Summary of Results for Test Particles*

In § 2 we described a numerical code that can follow the motion of a test particle in the presence of radiation in any stationary, axisymmetric spacetime. In the present paper we have verified this code by comparing results obtained using it with a variety of analytical results. We then used the code to compute the motion of test particles orbiting around slowly rotating radiation sources and gravitating masses. In future papers we will report results obtained using this code to analyze test particle motion around black holes and rapidly rotating neutron stars.

We analyzed test particle motion around a nonrotating radiation source and a spherical, nonrotating gravitating mass in § 3. This case can be treated analytically (see Appendix A and ML93). For particles in initially circular orbits, our numerical code gives results for the characteristic rates of loss of energy and angular momentum to the radiation field that agree with the exact analytical results to better than 5% (see Table 1).

In § 4 we considered test particle motion near rotating radiation sources in Schwarzschild spacetime and showed that if the velocity of the radiating matter is not too large there is a unique "equilibrium" angular momentum $u_{\phi 0}(r)$ for a particle in circular orbit at radius r at which the azimuthal component of the radiation force vanishes. The quantity $u_{\phi 0}(r)$ is independent of the luminosity of the radiation source and depends only weakly on the height h of the particle above the source and the width ϵ of the region that is radiating, varying by a factor ~ 2 as h varies from zero to infinity and as ϵ varies from zero to one (see Figs. 1*a* and 1*b*). Thus Ω_0, the equilibrium angular frequency as seen at radial infinity, varies approximately as r^{-2} at large r (see Fig. 1*c*). Both $u_{\phi 0}$ and Ω_0 are larger for radiating rings of smaller width. Surprisingly, the behavior of $u_{\phi 0}$ and Ω_0 as $h \to 0$ is qualitatively different for a radiating ring of any finite thickness than for ring of infinitesimal thickness. Thus in this sense (and perhaps in others) the two-dimensionality of a finite ring is significant.

In § 5 we derived exact analytical expressions for free fall in the Kerr metric and used them to verify the free-fall trajectories given by our numerical code. Even for rapidly rotating gravitating masses, particle trajectories computed using our code accurately match the exact trajectories (see Table 2).

We considered the effects of slow rotation of the radiation source and the gravitating mass in § 6 and § 7. In § 6 we obtained analytical expressions for the apparent angular shape of the star, the changes in photon frequency caused by frame-dragging and Doppler shifts, and the components $T^{\hat{t}\hat{\phi}}$ and $T^{\hat{r}\hat{\phi}}$ of the radiation stress-energy tensor, which are the only nonzero off-diagonal components. We also showed that Doppler shifts are typically much more important than

frame-dragging. In § 7 we presented numerical results for test-particle motion around a slowly rotating radiation source and gravitating mass (see Figs. 2, 3, and 4). Just as in the case of a static mass, which was treated in ML93, the initial radial velocity has little effect on the trajectories or the final specific energy and angular momentum, as long as $v^{\hat{r}} \ll v^{\hat{\phi}}$. The main new feature introduced by rotation is that the drag on particles in prograde orbits is less than it would be if the source were not rotating, because the radiation field carries angular momentum. However, the inspiral time is increased if the source is rotating, which offsets the lower drag rate. We find that the inspiral time increases faster than the drag decreases as the radiation energy density at the particle becomes lower; for the lowest specific intensities and narrowest radiation patterns we considered, the total energy and angular momentum transferred from the test particle to the radiation field are *greater* if the radiation source is rotating. These results demonstrate that radiation forces can be extremely important near accreting neutron stars.

8.2. *Application to Accretion Flows*

Under what conditions can the results obtained here be applied to accretion flows? The velocity of the accretion flow will be the same as the velocity of the test particles considered here if (1) the gravitational and radiation forces acting on the flow dominate all other forces, i.e., magnetic, pressure-gradient, and other forces are negligible, and (2) the radiation field is not significantly affected by its interaction with the accretion flow, i.e., if the accretion flow is optically thin (for a more complete discussion, see ML93 and LM95). If instead the accretion flow is optically thick, radiation forces will change the structure of the accretion flow, but the velocity will differ quantitatively from the velocity of test particles. Henceforth we assume that the gravitational and radiation forces acting on the flow dominate all other forces, and investigate at what accretion rates the accretion flow is optically thin in the radial direction.

Since we are restricting consideration to accretion flows that are optically thin in the vertical direction, flows that are geometrically thick in the vertical direction are necessarily optically thin in the radial direction. Flows that are geometrically thin may be optically thin or optically thick in the radial direction, depending on the structure of the flow. For a flow of half-thickness h, mass per particle m, and inward radial velocity v_r, the number density at radius r is

$$n = \frac{\dot{M}/m}{4\pi r^2 (h/r) v_r}, \tag{67}$$

where $\dot{M}$ is the mass accretion rate. Let $\dot{M}_0 \equiv (4\pi M m/\sigma)$, where σ is the scattering cross section. Then the vertical optical depth is

$$\tau_v = n\sigma h = \frac{\dot{M}}{\dot{M}_0}\left(\frac{M}{r}\right)\frac{1}{v_r}. \tag{68}$$

For example, if $v_r = 0.1$ at $r = 6M$, then $\tau_v < 1$ if $\dot{M} < 0.6\dot{M}_0$, which implies $\dot{M} < 10^{17}$ g s^{-1} for a fully ionized hydrogen plasma. The radial optical depth from r_1 to r_2 is

$$\tau_r = \frac{\dot{M}}{\dot{M}_0} M \int_{r_1}^{r_2} \left(\frac{r}{h}\right)\frac{dr}{r^2 v_r(r)}, \tag{69}$$

so, e.g., for $h/r = \text{const}$, $v_r(r) = \text{const.} = 0.1$, $r_1 = 6M$, and $r_2 = 12M$, one has $\tau_r < 1$ if $\dot{M} < 1.2(h/r)\dot{M}_0$.

Note that a flow may be optically thin in the vertical and radial directions in the presence of radiation even if it would be optically thick in the absence of such radiation, since removal of angular momentum by the radiation increases the radial velocity of the flow, thereby decreasing the optical depth ("induced transparency"). This effect allows radiation to penetrate further into the accretion flow and hence to affect a larger region of the flow than one would estimate from the velocity and density of the flow obtained by neglecting radiation forces. If the radial velocity profile computed using the test particle approximation gives $\tau_r < 1$, then this is the velocity profile of the accreting matter. Our numerical computations (see ML93 and § 7) give radial velocities near the star ~ 0.1–0.2 for intensities at the surface of the star ~ 0.05–0.5 times the critical surface intensity (see § 7). We therefore expect these velocity profiles to be accurate for $\dot{M} < 2 \times 10^{17}(h/r)$ g s^{-1} and intensities in this range.

8.3. *Application to Nuclear-Powered Sources*

Consider now a source with a high luminosity that is produced, at least temporarily, by some process other than accretion, such as nuclear burning in the outer layers of the star. As an example, some type I X-ray burst sources have burst luminosities $\sim L_E^\infty$ for many minutes (see Lewin, van Paradijs, & Taam 1993). During such a burst the inflow time near the star is a millisecond or less, much shorter than the duration of the burst. Hence interaction of the burst radiation with the accretion flow will establish a quasi-steady inflow near the star, and the velocity structure of the inflow will therefore track gradual changes in the burst luminosity.

From the discussion in § 8.2, we expect the velocity profiles presented in § 7 to be accurate when $\dot{M}$ is less than $\sim 2 \times 10^{17}(h/r)$ g s^{-1}. At these mass accretion rates the accreting fluid will transfer most of its energy and angular momentum to the radiation field before hitting the stellar surface and the inflow velocity will be greatly increased by radiation drag (see Figs. 2, 3, and 4). As a result, the accretion rate may increase temporarily (see Walker & Mészáros 1989; Walker 1992). On the other hand, if the luminosity becomes greater than the local critical luminosity, the accretion flow will be halted (see LM95). Hence the accretion rate may either increase or decrease during the burst, depending on the instantaneous luminosity.

8.4. *Application to Accretion-Powered Sources*

In sources in which the luminosity is produced primarily by accretion, the specific angular momentum and energy of the accreting matter at the stellar surface is determined by the fraction of its energy and angular momentum that has been transferred to the radiation field. Angular, special relativistic, and general relativistic effects influence this fraction differently from the way they influence the *rates* of energy and angular momentum loss. We illustrate this with the following example.

Suppose there is a radius r_0 that characterizes the interaction of the radiation with the accretion flow, in the sense that the angular momentum of the scattered radiation as measured at infinity is equal to that calculated by assuming that all photons scatter once, at $r = r_0$. This approximation will be inappropriate if a large fraction of the photons leaving the star eventually diffuse back to the stellar surface, i.e., if back-heating is important. We expect back-heating to

be unimportant if $\tau_r \lesssim 1$, since the first scattering will then typically occur a large distance from the star and hence the probability that the photon is scattered back to the stellar surface will be small. We therefore again restrict consideration to accretion rates $\dot{M} \lesssim 2 \times 10^{17}(h/r)$ g s^{-1}, or equivalently $L \lesssim 0.1(h/r)L_E^{\infty}$.

Consider first the effect of radiation interacting with matter orbiting in flat spacetime near a fictional point source of radiation with a luminosity equal to $\epsilon\dot{M}c^2$, where ϵ is the "efficiency" with which the source produces radiation. The specific angular momentum of matter orbiting at r_0 is $u_\phi(r_0) = r_0 v_\phi(r_0)$. If a fraction f of the radiation coming from the source interacts with the matter, then after scattering the radiation carries an angular momentum flux

$$\dot{J}_{\rm ph} \approx r_0\left(\frac{fL}{c}\right)\left[\frac{v_\phi(r_0)}{c}\right] = f\epsilon\dot{M}r_0 v_\phi(r_0) = f\epsilon\dot{J}_m\,, \qquad (70)$$

where $\dot{J}_m$ is the flux of angular momentum carried inward by the matter at $r = r_0$. Thus, a fraction $\sim f\epsilon$ of the angular momentum of the accreting matter is carried away by the radiation, which is a fraction ~ 0.2–0.3 for $f \sim 1$ and typical accretion efficiencies.

Near a radiating neutron star, the angular, special relativistic, and general relativistic effects discussed in § 2 and Appendix A increase the ratio $\dot{J}_{\rm ph}/\dot{J}_m$ compared to the ratio for a point source in the Newtonian approximation. However, in contrast to the drag *rate*, which depends on both the angular momentum transferred per scattering event and the scattering rate, the *fraction* of the angular momentum of the accreting matter that is transferred to the radiation field does not depend on the scattering rate. Therefore, only effects that increase the angular momentum transferred per scattering event affect the fraction of the angular momentum of the accreting matter that is carried away by the radiation field.

For example, at the surface of the star, angular effects increase the angular momentum loss rate by a factor of 8/3 compared to the loss rate near a point source: a factor of 2 from the increase in the photon number density (which increases the rate of scattering) and a factor of 4/3 from the increase in the angular momentum removed by each photon. In contrast, angular effects increase the fraction of the angular momentum of the matter that is lost to the radiation field by 4/3.

General relativistic effects increase the angular momentum loss rate by two factors of the redshift (see § 3) but increase the fraction of the angular momentum that is lost by only one factor of the redshift. To see this, note that gravitational bending of light rays in the Schwarzschild spacetime causes the impact parameter of escaping photons to be one factor of the redshift greater at radial infinity than in flat spacetime. Thus, for a given flux at radial infinity the flux of angular momentum at infinity carried by a given radiation energy flux is greater by just one factor of the redshift. For matter at the surface of a star of radius $6M$, this increases the fractional loss by a factor $(3/2)^{1/2}$. The special relativistic forward beaming of scattered radiation increases the fractional loss of angular momentum the same as the loss rate, by a factor of up to $\sim 4/3$.

As a concrete example, the angular momentum loss rate for a particle in Keplerian orbit at $r = 6M$ is $(8/3) \times (4/3) \times (3/2) \approx 5.3$ times the loss rate near a point source in the Newtonian approximation, whereas the fraction of the angular momentum lost from a fluid element in Keplerian orbit at the surface of a star of radius $R = 6M$ is $(4/3) \times (4/3) \times (3/2)^{1/2} \approx 2.2$ times the fraction lost near a point source in flat spacetime. Thus, although the fractional loss of angular momentum is not increased as much as the loss rate, it can be more than twice as much as near a point source in the Newtonian approximation.

The average velocity of matter in the boundary layer at the surface of a slowly rotating neutron star is of order half the velocity of matter in orbit just outside it. Hence, scattering of radiation produced in the boundary layer, as well as scattering of radiation coming from the stellar surface, will brake the orbital motion of matter in the disk. If $f \sim 1$ and the accretion efficiency ϵ is ~ 0.2–0.3, radiation can carry away a fraction ~ 0.3–0.5 of the angular momentum of the accreting fluid, significantly increasing the radial velocity of the inflow (see Figs. 2, 3, and 4) and decreasing its optical depth.

In sources in which the luminosity is produced primarily by accretion, transfer of energy from the accretion flow to the radiation field reduces the luminosity produced at or near the stellar surface. As we have shown, radiation emitted by a slowly rotating neutron star and scattered by matter orbiting near the surface removes up to a factor 4/3 more angular momentum than is removed by radiation emitted directly by the matter orbiting there. Thus the decrease in the luminosity of the stellar surface caused by transfer of energy from the accreting matter to the escaping radiation diminishes slightly the effect of radiation on the accretion flow near an accretion-powered star when compared to the effect near a bursting star of the same luminosity. However, the main difference is that the luminosity of a nuclear-powered star can be near-critical and can therefore have a very strong effect on the accretion flow, even if the accretion rate is relatively low and is therefore optically thin.

8.5. *Implications for Spin-Up of Slowly Rotating Neutron Stars*

The gravitational potential energy per unit mass released by accretion onto the surface of a neutron star is $\sim 0.2c^2$, whereas the energy per unit mass released by thermonuclear fusion is only $\sim 0.007c^2$. Hence the time-averaged luminosity of an accreting neutron star is dominated by the gravitational energy release. The average rate at which angular momentum is carried away by radiation (or a wind) is therefore dominated by the rate of angular momentum loss between any nuclear outbursts, and the average rate of spin-up of an accreting neutron star is almost independent of the details of any outbursts. Thus, in computing the long-term spin evolution of neutron stars it is a good approximation to assume that the neutron star is always accretion-powered. The results of § 8.4 are therefore relevant.

As mentioned above, the average velocity of matter in the boundary layer at the surface of a slowly rotating neutron star is of order half the velocity of the matter in orbit just outside it. Therefore, scattering of radiation produced in the boundary layer, as well as scattering of radiation coming from the stellar surface, will remove angular momentum from the matter in the disk outside the boundary layer. The numerical computations summarized in § 7 indicate that the radiation will carry away a fraction $\sim 2f\epsilon$ of the angular momentum of the accreting matter, thereby decreasing the

spin-up rate by $\sim 30\%$–50% (if $f \sim 1$) compared to the rate if radiation forces could be neglected.

An important question is, what fraction of the angular momentum of matter accreting onto a rapidly rotating neutron star is lost to radiation? Even if this fraction is small, it will decrease the maximum rotation rate of neutron star and may prevent emission of gravitational radiation from neutron stars rotating near breakup; we will address these and other questions related to fast rotation in a future paper.

This work was begun while both authors were visiting Nordita. We are grateful to the staffs of Nordita and the Niels Bohr Institute and especially the then director of Nordita, Christopher Pethick, for their warm hospitality and help during our visit. F. K. L. also thanks the staff of the University of Copenhagen Observatory and especially its director, Henning Jørgensen, for their assistance and hospitality. This work was supported in part by NSF grant AST 93-15133 and NASA grants NAGW 1583 and NAG 5-2925 at the University of Illinois, NASA grant NAG 5-2868 at the University of Chicago, and through the *Compton* Fellowship Program, by NASA grant NAS 5-28543.

APPENDIX A

EFFECTS CONTRIBUTING TO THE ANGULAR MOMENTUM LOSS RATE IN SCHWARZSCHILD SPACETIME

From equation (3), the ϕ-component of the relativistic equation of motion is

$$a^{\phi} = f^{\phi}/m \,, \tag{A1}$$

where $f^{\phi} = \sigma F^{\phi}$, $F^{\phi} = -(T^{\mu\phi}u_{\mu} + u^{\phi}T^{\mu\beta}u_{\mu}u_{\beta})$ (see eqs. [6] and [7]). In the Schwarzschild spacetime with $u_{\theta} = u^{\theta} = 0$,

$$a^{\phi} = \frac{du^{\phi}}{d\tau} + \Gamma^{\phi}_{\mu\nu}u^{\mu}u^{\nu} = \frac{du^{\phi}}{d\tau} + \frac{2}{r}u^{\phi}u^{r} \,. \tag{A2}$$

The rate of change of angular momentum is

$$\frac{du_{\phi}}{d\tau} = \frac{d(r^2u^{\phi})}{d\tau} = r^2\frac{du^{\phi}}{d\tau} + 2ru^{\phi}u^{r} = r^2a^{\phi} \,. \tag{A3}$$

For particle motion in the ϕ-r plane and radiation from a nonrotating star, the important nonzero components of the radiation stress-energy tensor are $T^{tt} = (1 - 2M/r)^{-1}T^{\hat{t}\hat{t}}$, $T^{tr} = T^{rt} = T^{\hat{t}\hat{r}}$, $T^{rr} = (1 - 2M/r)T^{\hat{r}\hat{r}}$, and $T^{\phi\phi} = (1/r^2)T^{\hat{\phi}\hat{\phi}}$. Thus,

$$F^{\phi} = -T^{\phi\phi}u_{\phi} - u^{\phi}(T^{tt}u_t^2 + 2T^{tr}u_t u_r + T^{rr}u_r^2 + T^{\phi\phi}u_{\phi}^2) \,. \tag{A4}$$

From $u^{\alpha}u_{\alpha} = -1$, we find $u_{\phi}^2 = r^2[-1 + (1 - 2M/r)^{-1}u_t^2 - (1 - 2M/r)u_r^2]$. Further manipulation of equation (A4) then yields

$$F^{\phi} = -T^{\phi\phi}u_{\phi} + u^{\phi}T^{\hat{\phi}\hat{\phi}} - u^{\phi}\frac{1}{1 - 2M/r}u_t^2\left[T^{\hat{t}\hat{t}} + 2\left(1 - \frac{2M}{r}\right)\frac{u_r}{u_t}T^{\hat{t}\hat{r}} + \left(1 - \frac{2M}{r}\right)^2T^{\hat{r}\hat{r}}\frac{u_r^2}{u_t^2} + T^{\hat{\phi}\hat{\phi}} - \left(1 - \frac{2M}{r}\right)^2T^{\hat{\phi}\hat{\phi}}\frac{u_r^2}{u_t^2}\right] . \tag{A5}$$

If the test particle at radius r has a total velocity β and moves at an angle ψ relative to the azimuthal direction as seen by a local static observer, then $v^{\hat{r}} = -\beta \sin\psi$ and $u_r/u_t = -v^{\hat{r}}/(1 - 2M/r) = \beta \sin\psi/(1 - 2M/r)$. Since $T^{\phi\phi}u_{\phi} = u^{\phi}T^{\hat{\phi}\hat{\phi}}$, we then have

$$F^{\phi} = -\frac{1}{r^2(1 - 2M/r)}u_t^2u_{\phi}[T^{\hat{t}\hat{t}} + 2\beta \sin\psi T^{\hat{t}\hat{r}} + (1 - \beta^2 \sin^2\psi)T^{\hat{\phi}\hat{\phi}} + \beta^2 \sin^2\psi T^{\hat{r}\hat{r}}] \,. \tag{A6}$$

From equation (11),

$$T^{\hat{t}\hat{t}} = 2\pi I(1 - \cos\alpha_0) \,, \quad T^{\hat{t}\hat{r}} = \pi I \sin^2\alpha_0 \,, \quad T^{\hat{r}\hat{r}} = \tfrac{2}{3}\pi I(1 - \cos^3\alpha_0) \,, \quad \text{and} \quad T^{\hat{\phi}\hat{\phi}} = \tfrac{1}{3}\pi I(\cos^3\alpha_0 - 3\cos\alpha_0 + 2) \,. \tag{A7}$$

For a nonrotating spherical source of radius R in the Schwarzschild spacetime emitting radiation uniformly and isotropically as seen by an observer on the surface of the source, the specific intensity depends only on the radius (see LM95) and is

$$I(r) = \frac{(1 - 2M/r)}{(1 - 2M/r)^2}\frac{mM}{\pi\sigma R^2}\left(\frac{L^{\infty}}{L_{\rm E}^{\infty}}\right) , \tag{A8}$$

where $L_{\rm E}^{\infty}$ is defined in § 3. Collecting terms, and writing $l \equiv u_{\phi}$ and $1 - \tilde{E}_b \equiv -u_t$, we have finally

$$\frac{1}{l}\frac{dl}{d\tau} = -f(\alpha, \psi, \beta)(1 - \tilde{E}_b)^2\frac{M}{3R^2}\frac{(1 - 2M/R)}{(1 - 2M/r)^3}\left(\frac{L^{\infty}}{L_{\rm E}^{\infty}}\right) , \tag{A9}$$

where

$$f(\alpha, \psi, \beta) \equiv [8 - 9\cos\alpha + \cos^3\alpha + 3\beta \sin\psi \sin^2\alpha(2 + \beta \sin\psi \cos\alpha)] \,. \tag{A10}$$

Equation (13) can be derived similarly.

Note that the angular factor $f(\alpha, \psi, \beta)$ is minimized for circular orbits ($\psi = 0$), so that for a given locally measured velocity β, the characteristic angular momentum loss rate is greater for noncircular orbits than for circular orbits. However, this correction is relatively small. For a particle with $\beta = 0.5$ at the surface of a star of radius $R = 6M$, the angular factor f is 11 for near-radial motion ($\psi \to \pi/2$) compared to 8 for purely azimuthal motion ($\psi = 0$). The factor f is 3 for circular motion around a point source, so the loss rate is enhanced by as much as a factor of 8/3 for motion near the stellar surface. Our expression for f at $\psi = 0$ is identical to that derived by Guess (1962) for orbital motion in the flat-space, slow-particle motion approximation. Guess attributed the factor 8/3 to a combination of Doppler shifts and aberration effects, implying that this enhancement should also occur for a single scattering. However, our analysis shows that for a single scattering, the average enhancement factor can be at most 4/3. The extra factor of 2 arises because, for a fixed flux or luminosity at infinity, the energy density (and hence the number density of photons) at the surface of a source of radius R is twice that at radius R from a point source. The reason is that photons from a point source are all traveling radially, whereas many of the photons from an extended source are traveling obliquely to the radial direction so that for the same flux there are more photons. Thus, interactions happen twice as often and each interaction removes, on average, 4/3 times as much angular momentum as for a point source.

The second factor that increases the loss rate and loss per scattering compared to the losses for a Newtonian point source is relativistic beaming. In Schwarzschild spacetime, $u_t^2/(1 - 2M/r) = \gamma^2$, as may be verified using the definitions of local radial and azimuthal velocities and the identity $u^\alpha u_\alpha = -1$. Relativistic beaming increases both the loss rate and the angular momentum lost in a single scattering by the same factor γ^2; for example, a particle moving in a circular orbit ($\psi = 0$) in a vacuum at the surface of a nonradiating star with radius $R = 6M$ has $\beta = 0.5$, so $\gamma^2 = 4/3$.

The last effect to enhance losses is the gravitational bending of light rays. A photon scattered by a particle at a finite radius r is afterward deflected by the gravitational field, so that its impact parameter at infinity (and hence its specific angular momentum) is greater than at r by one factor of the redshift, $(1 - 2M/r)^{-1/2}$. Thus, for a fixed luminosity or photon energy at infinity, the ratio of the angular momentum loss to the angular momentum of the particle (and thus the loss in a single scattering) is larger by one factor of the redshift. By contrast, the loss *rate* is enhanced by two factors of the redshift, because the scattering frequency is also increased by one redshift factor.

To summarize, the loss *rate* near the surface of a relativistic star is greater than the loss rate near a point source in the Newtonian approximation by up to a factor ~ 5 (8/3 from the finite angular size of the star, 4/3 from relativistic beaming, and ~ 1.2–2 from two factors of the redshift), whereas the angular momentum loss *per scattering* is only greater by up to a factor ~ 2 (4/3 from the finite angular size of the star, 4/3 from relativistic beaming, and ~ 1.2–1.5 from one factor of the redshift).

APPENDIX B

ABSENCE OF FIRST-ORDER ROTATION EFFECTS

Under what circumstances are the radial component of the radiation flux and the diagonal components of the stress-energy tensor at radius r in the equatorial plane unchanged to first order in the rotation rates of the gravitating mass and radiation source? Here we show that if the emitted radiation is front-back symmetric with respect to the directions of motion of the radiating matter as seen by a comoving local observer and the radiation source is axisymmetric, then changing the direction of rotation of both the gravitating mass and radiation source does not affect $T^{\hat{t}\hat{r}}$, $T^{\hat{t}\hat{t}}$, $T^{\hat{r}\hat{r}}$, $T^{\hat{\theta}\hat{\theta}}$, or $T^{\hat{\phi}\hat{\phi}}$.

First we show that if the ray defined by the angles $(\tilde{a}, \tilde{b})$ in the local orthonormal frame at radius r (see eq. [10]) propagating in a spacetime with rotational parameter j originates from the stellar surface at $(\theta[R], \phi[R])$, then the ray with local angles $(\tilde{a}, -\tilde{b})$ in a spacetime with rotational parameter $-j$ originates at $(\theta[R], -\phi[R])$.

From equation (10), holding $\tilde{a}$ constant while changing the sign of $\tilde{b}$ keeps $u^{\hat{r}}/u^{\hat{t}}$ and $u^{\hat{\theta}}/u^{\hat{t}}$ constant but changes the sign of $u^{\hat{\phi}}/u^{\hat{t}}$. The specific angular momentum of a photon is

$$l = -\frac{u_\phi}{u_t} = -\frac{e_{\hat{\phi}}^{\hat{\phi}} u_{\hat{\phi}}}{e_{\hat{t}}^{\hat{t}} u_{\hat{t}} + e_{\hat{t}}^{\hat{\phi}} u_{\hat{\phi}}} = -\frac{e_{\hat{\phi}}^{\hat{\phi}} u^{\hat{\phi}}}{-e_{\hat{t}}^{\hat{t}} u^{\hat{t}} + e_{\hat{t}}^{\hat{\phi}} u^{\hat{\phi}}} = \frac{e_{\hat{\phi}}^{\hat{\phi}} (u^{\hat{\phi}}/u^{\hat{t}})}{e_{\hat{t}}^{\hat{t}} - e_{\hat{t}}^{\hat{\phi}} (u^{\hat{\phi}}/u^{\hat{t}})} . \tag{B1}$$

Since to first order $e_{\hat{\phi}}^{\hat{\phi}}$ and $e_{\hat{t}}^{\hat{t}}$ are independent of j whereas $e_{\hat{t}}^{\hat{\phi}} \propto j$, equation (B1) shows that $l \to -l$ when $j \to -j$ and $\tilde{b} \to -\tilde{b}$. To $\mathcal{O}(j)$, the change in the angular position of a photon with radius is given by (Bardeen et al. 1972)

$$\frac{d\theta}{dr} = \pm \frac{(q - l^2 \cot^2 \theta)^{1/2}}{(V_r/u_t^2)^{1/2}} \tag{B2}$$

and

$$\frac{d\phi}{dr} = \frac{-jM + l \csc^2 \theta + jM/(1 - 2M/r)}{(V_r/u_t^2)^{1/2}} , \tag{B3}$$

where V_r is defined in equation (56). Equations (B2) and (B3) show that when $j \to -j$ and $l \to -l$, θ is unchanged whereas ϕ changes sign, so that $\theta(R) \to \theta(R)$ and $\phi(R) \to -\phi(R)$.

A reversal of this argument shows that the converse is also true: when $\theta(R) \to \theta(R)$, $\phi(R) \to -\phi(R)$, and $j \to -j$, the direction of the ray as seen by an LNRF observer at r changes from $(\tilde{a}, \tilde{b})$ to $(\tilde{a}, -\tilde{b})$. Thus, e.g., if the source is an axisymmetric ring at some fixed θ, the angular extent of the ring in $\tilde{b}$ is reversed by changing the sign of j, so that if the ring originally appeared to

extend from $\tilde{b}_1$ to $\tilde{b}_2$, after $j \to -j$ the ring will appear to extend from $-\tilde{b}_2$ to $-\tilde{b}_1$. The range in $\tilde{a}$ is unchanged, so if at a given angle $\tilde{b}_0$ the ring originally extended from $\tilde{a}$ to $\tilde{a} + \Delta\tilde{a}$, after $j \to -j$ the ring will extend from $\tilde{a}$ to $\tilde{a} + \Delta\tilde{a}$ at $-\tilde{b}_0$.

Consider now the radial component of the radiation flux from an axisymmetric ring at constant θ but varying ϕ. We suppose the thickness of the ring is small but finite. Let the apparent angular range in $\tilde{b}$ be from $\tilde{b}_1$ to $\tilde{b}_2$, and for a given $\tilde{b}$ let the range in $\tilde{a}$ be from $\tilde{a}(\tilde{b})$ to $\tilde{a}(\tilde{b}) + \Delta\tilde{a}(\tilde{b})$. Then

$$T^{\hat{r}\hat{r}}(\text{orig}) = \int_{\tilde{b}_1}^{\tilde{b}_2} \int_{\tilde{a}(\tilde{b})}^{\tilde{a}(\tilde{b})+\Delta\tilde{a}(\tilde{b})} I(r, \tilde{a}, \tilde{b}) \sin\tilde{a} \cos\tilde{a}\, d\tilde{a}\, d\tilde{b}\,, \tag{B4}$$

where the notation (orig) indicates that the gravitating mass and radiation source are rotating in their original directions, which could be opposite to one another.

For rotation in the opposite directions, the signs of j *and* the velocity v of the radiating matter seen by an observer in the LNRF at the stellar surface change; if the sign of j/v is unchanged, then from equation (60) the magnitude of the frequency shift is unchanged. Thus, the transformations $(j > 0, v > 0) \to (j < 0, v < 0)$ and $(j < 0, v > 0) \to (j > 0, v < 0)$ leave the magnitude of the frequency shift unchanged, whereas $(j > 0, v < 0) \to (j > 0, v > 0)$ does not. The radial component of the radiation flux $T^{\hat{r}\hat{r}}(\text{rev})$ is

$$T^{\hat{r}\hat{r}}(\text{rev}) = \int_{-\tilde{b}_2}^{-\tilde{b}_1} \int_{\tilde{a}(\tilde{b})}^{\tilde{a}(\tilde{b})+\Delta\tilde{a}(\tilde{b})} I(r, \tilde{a}, \tilde{b}) \sin\tilde{a} \cos\tilde{a}\, d\tilde{a}\, d\tilde{b}\,. \tag{B5}$$

Making the change $\tilde{b} \to -\tilde{b}$ and using $\tilde{a}(\tilde{b}) = \tilde{a}(-\tilde{b})$ gives

$$T^{\hat{r}\hat{r}}(\text{rev}) = \int_{\tilde{b}_1}^{\tilde{b}_2} \int_{\tilde{a}(\tilde{b})}^{\tilde{a}(\tilde{b})+\Delta\tilde{a}(\tilde{b})} I(r, \tilde{a}, -\tilde{b}) \sin\tilde{a} \cos\tilde{a}\, d\tilde{a}\, d\tilde{b}\,, \tag{B6}$$

so $T^{\hat{r}\hat{r}}(\text{rev}) = T^{\hat{r}\hat{r}}(\text{orig})$ if $I(r, \tilde{a}, \tilde{b}) = I(r, \tilde{a}, -\tilde{b})$.

From equation (58), the $\mathcal{O}(j)$ term in the Doppler shift is proportional to $v \sin\tilde{b}$. Since both v and $\sin\tilde{b}$ change sign when $j \to -j$ and $v \to -v$, the Doppler shift has the same value after rotation as it did before. Similarly, from equation (59), the $\mathcal{O}(j)$ term in the LNRF frequency shift is proportional to $j \sin\tilde{b}$, which also is unchanged by rotation. Thus, from equation (60),

$$\frac{I(r, \tilde{a}, \tilde{b})}{I(r, \tilde{a}, -\tilde{b})} = \frac{I(R, \theta, \phi, \tilde{a}[R], \tilde{b}[R])}{I(R, \theta, -\phi, \tilde{a}[R], -\tilde{b}[R])}\,, \tag{B7}$$

where $I(R, \theta, \phi, \tilde{a}[R], \tilde{b}[R])$ is the specific intensity seen in the direction $(\tilde{a}[R], \tilde{b}[R])$ by an observer in the LNRF at the position (θ, ϕ) on the stellar surface. If the radiation, as seen by an observer comoving with the emitting surface, is back-front symmetric about the (r, θ) plane, then $I(R, \theta, \phi, \tilde{a}[R], \tilde{b}[R]) = I(R, \theta, -\phi, \tilde{a}[R], -\tilde{b}[R])$ and hence $T^{\hat{r}\hat{r}}(\text{orig}) = T^{\hat{r}\hat{r}}(\text{rev})$. This symmetry holds in part because $n^{\hat{t}}n^{\hat{r}} = \cos\tilde{a}$ is even in $\tilde{b}$ (see eqs.[10] and [11]). Likewise, $n^{\hat{\alpha}}n^{\hat{\alpha}}$ is even in $\tilde{b}$ for $\alpha = t, r, \theta$, or ϕ, so $T^{\hat{\alpha}\hat{\alpha}}$ is unchanged by changing the sign of both j and v if the source is axisymmetric and emission is locally front-back symmetric. By contrast, $n^{\hat{t}}n^{\hat{\phi}} = \sin\tilde{a} \sin\tilde{b}$ is odd in $\tilde{b}$, so $T^{\hat{t}\hat{\phi}}$ changes sign under reversal of both rotations.

Because j and v are signed quantities, dependence of a quantity on odd orders of j and v implies a change in that quantity when $j \to -j$ and $v \to -v$. Thus, if a quantity is unchanged when $j \to -j$ and $v \to -v$, it does not depend on odd orders of j and v, and in particular does not have first-order corrections in j and v. The argument given here therefore proves that if a source is axisymmetric and front-back symmetric, then $T^{\hat{r}\hat{r}}$, $T^{\hat{t}\hat{t}}$, $T^{\hat{r}\hat{t}}$, $T^{\hat{\theta}\hat{\theta}}$, $T^{\hat{\phi}\hat{\phi}}$, $T^{\hat{t}\hat{\theta}}$, and $T^{\hat{r}\hat{\theta}}$ do not depend on j and ϕ to first order, whereas there are first-order terms in $T^{\hat{t}\hat{\phi}}$, $T^{\hat{r}\hat{\phi}}$, and $T^{\hat{\theta}\hat{\phi}}$.

REFERENCES

Abramowicz, M. A., Ellis, G. F. R., & Lanza, A. 1990, ApJ, 361, 470 (AEL)
Bardeen, J. M. 1970, ApJ, 162, 71
Bardeen, J. M., Press, W. H., & Teukolsky, S. A. 1972, ApJ, 178, 347
Biehle, G., & Blandford, R. D. 1993, ApJ, 411, 302
Cook, G. B., Shapiro, S. L., & Teukolsky, S. A. 1994, ApJ, 424, 823
Czerny, B., Czerny, M., & Grindlay, J. E. 1986, ApJ, 311, 241
Ebisawa, K., Mitsuda, K., & Hanawa, T. 1991, ApJ, 367, 213
Fortner, B. A., Lamb, F. K., & Miller, G. S. 1989, Nature, 342, 775
Friedman, J. L., Ipser, J. R., & Parker, L. 1986, ApJ, 304, 115
Fu, A., & Taam, R. E. 1990, ApJ, 353, 205
Guess, A. W. 1962, ApJ, 135, 855
Hanawa, T. 1989, ApJ, 341, 948
Hartle, J. B., & Thorne, K. S. 1968, ApJ, 153, 807
Kluzniak, W., & Wagoner, R. V. 1985, ApJ, 297, 548
Kluzniak, W., & Wilson, J. R. 1991, ApJ, 372, L87
Lamb, F. K., & Miller, M. C. 1995, ApJ, 439, 828 (LM95)
Lewin, W. H. G., van Paradijs, J., & Taam, R. E. 1993, Space Sci. Rev., 62, 223
Miller, M. C., & Lamb, F. K. 1993, ApJ, 413, L43 (ML93)
Sunyaev, R. A., & Shakura, N. I. 1986, AZhPis'ma, 12, 286
Taylor, J. H., Manchester, R. N., Lyne, A. G., & Camilo, F. 1995, electronic catalog of pulsars, available via anonymous ftp from pulsar.princeton.edu, directory pub/catalog
van Paradijs, J. 1991, in Neutron Stars: Theory and Observation, ed. J. Ventura & D. Pines (Dordrecht: Kluwer), 245
Walker, M. A. 1992, ApJ, 385, 642
Walker, M. A., & Mészáros, P. 1989, ApJ, 346, 844